Bioactive Materials 28 (2023) 311–325

Contents lists available at ScienceDirect

Bioactive Materials

journal homepage: www.keaipublishing.com/en/journals/bioactive-materials

Highly resilient and fatigue-resistant poly(4-methyl-ε-caprolactone) porous scaffold fabricated via thiol-yne photo-crosslinking/salt-templating for soft tissue regeneration

Zhaochuang Wang [a,1], Wenhao Zhang [c,1], Guo Bai [c,1], Qiaohui Lu [b], Xiaoyu Li [a], Yan Zhou [b,**], Chi Yang [c,***], Yan Xiao [a,****], Meidong Lang [a,*]

[a] Shanghai Key Laboratory of Advanced Polymeric Materials, Key Laboratory for Ultrafine Materials of Ministry of Education, School of Materials Science and Engineering, East China University of Science and Technology, Shanghai, 200237, PR China
[b] State Key Laboratory of Bioreactor Engineering, School of Biotechnology, East China University of Science and Technology, Shanghai, 200237, PR China
[c] Shanghai Key Laboratory of Stomatology, Shanghai Research Institute of Stomatology, Department of Oral Surgery of Ninth People's Hospital, College of Stomatology, Shanghai Jiao Tong University School of Medicine, Shanghai, 200011, PR China

ARTICLE INFO

Keywords:
Elastomeric scaffold
Thiol-yne photo-crosslinking
Fatigue resistance
Tissue regeneration

ABSTRACT

Elastomeric scaffolds, individually customized to mimic the structural and mechanical properties of natural tissues have been used for tissue regeneration. In this regard, polyester elastic scaffolds with tunable mechanical properties and exceptional biological properties have been reported to provide mechanical support and structural integrity for tissue repair. Herein, poly(4-methyl-ε-caprolactone) (PMCL) was first double-terminated by alkynylation (PMCL-DY) as a liquid precursor at room temperature. Subsequently, three-dimensional porous scaffolds with custom shapes were fabricated from PMCL-DY via thiol-yne photocrosslinking using a practical salt template method. By manipulating the M_n of the precursor, the modulus of compression of the scaffold was easily adjusted. As evidenced by the complete recovery from 90% compression, the rapid recovery rate of >500 mm min^{-1}, the extremely low energy loss coefficient of <0.1, and the superior fatigue resistance, the PMCL20-DY porous scaffold was confirmed to harbor excellent elastic properties. In addition, the high resilience of the scaffold was confirmed to endow it with a minimally invasive application potential. In vitro testing revealed that the 3D porous scaffold was biocompatible with rat bone marrow stromal cells (BMSCs), inducing BMSCs to differentiate into chondrogenic cells. In addition, the elastic porous scaffold demonstrated good regenerative efficiency in a 12-week rabbit cartilage defect model. Thus, the novel polyester scaffold with adaptable mechanical properties may have extensive applications in soft tissue regeneration.

1. Introduction

Tissue engineering scaffolds have been custom-made for the repair and reconstruction of damaged tissues and organs by providing a suitable growth environment for cells and a mechanical support for regeneration with minimal immune response [1–4]. Due to the mechanically dynamic loading environment of the human body, the implanted scaffold could follow the changes in tissue deformation without mechanically irritating the surrounding tissues and recover from various deformations over time to provide stable support [5]. In an ideal situation, tissue-engineered scaffolds composed of soft, elastic biodegradable polymers facilitate the replacement of elastin networks in injured tissues, providing mechanical support and structural integrity [6]. Although many elastic scaffolds with biocompatible and biodegradable properties have been reported [7–13], the development of biodegradable elastomers that can readily recover from large deformations over

Peer review under responsibility of KeAi Communications Co., Ltd.
* Corresponding author.
** Corresponding author.
*** Corresponding author.
**** Corresponding author.
E-mail addresses: zhouyan@ecust.edu.cn (Y. Zhou), yangchi63@hotmail.com (C. Yang), yxiao@ecust.edu.cn (Y. Xiao), mdlang@ecust.edu.cn (M. Lang).
[1] These authors contributed equally to this work.

https://doi.org/10.1016/j.bioactmat.2023.05.020
Received 7 March 2023; Received in revised form 12 May 2023; Accepted 30 May 2023

long-term cycling and provide stable mechanical support remains a significant challenge.

Polyester elastomers have been extensively studied in soft tissue regeneration due to their tunable mechanical properties and outstanding biological properties [14]. For instance, elastomeric poly (lactide-*co*-caprolactone) (PLCL) and poly(glycolide-*co*-caprolactone) (PGCL) were developed by copolymerizing the soft segment of PCL with the hard segments of PLA and PGA, respectively [15–17]. These copolyesters with the appropriate ratio of soft to hard components were primarily manufactured for use as tendon, muscle, bone, and cartilage tissue engineering scaffolds [18–21]. However, the limited elasticity of these scaffolds makes them susceptible to permanent deformation and partial loss of support function when subjected to dynamic loading over extended time periods. Other chemically cross-linked materials, such as poly(glycerol sebacate) (PGS) and poly(diol citrate) (PDC), have been used for cardiac patches, tracheal substitutes, vascular and cartilage scaffolds [22–29]. In this regard, Wang et al., synthesized palmitic acid-modified PGS (PPGS) to slow the degradation of PGS to coincide with tissue regeneration. In a rat carotid artery model, PPGS with greater elasticity demonstrated greater patency, less inflammation, and regenerated tissue with a protein distribution similar to that of natural arteries [30]. In addition, Zhao et al., created 3D-pritned PGS-PCL scaffolds comprising a stacked structure of regular crossover filaments and interconnected micropores by co-blending PGS with PCL, which effectively protected and improved cardiac function in a rat myocardial infarction model, thereby offering a promising strategy for myocardial remodeling [31]. However, network formation by polycondensation frequently necessitates harsh conditions, such as high temperature or extended reaction time, even though the components of PGS-based elastomer are versatile.

Given the ease of radical polymerization, the use of poly(glycerol sebacate) acrylate (PGSA) has aided in overcoming a major bottleneck in PGS production and streamlined the reaction process [32,33]. Other acrylated (co)polyesters have also been extensively studied for photo-initiated scaffold processing with spatiotemporal control and environmental friendliness [34,35]. However, the oxygen-blocking properties of acrylic radical polymerization result in a low conversion rate (60–90%) and uncured groups may be potentially cytotoxic [36]. Meanwhile, the non-uniform network topology that results from the radical polymerization mechanism of acrylates produces inhomogeneous networks that are susceptible to structural damage under prolonged dynamic loading of the human body [37]. Ideally, we expect the cross-linking process of scaffolds to be simple and efficient, with homogeneous networks capable of withstanding dynamic loading. Due to its orthogonal step-growth polymerization mechanism, thiol-ene/yne metal-free click chemistry enables the easy construction of homogeneous networks with minimal spatial and topological defects [38–41]. Thus, using thiol-ene click chemistry, Burdick et al., synthesized norbornene-functionalized PGS that were crosslinked with a tetra-thiol cross-linker to finally yield elastomers [42]. The elastomer could be cross-linked in less than a minute and 3D-printed to create complex scaffolds for biomedical applications [42]. In addition, Vlierberghe et al., reported the conversion from a chain-growth mechanism of acrylate crosslinking to a step-growth polymerization mechanism of thiol-ene/yne crosslinking by altering the end group functionality of poly(ε-caprolactone) (PCL) to construct a homogeneous network, which significantly increased the strength and elongation at break [43]. However, the semi-crystalline precursors of PGS/PCL generated elastomers with brittle fracture and poor dynamic loading resistance. In previous research, “liquid” poly (4-methyl-ε-caprolactone) diacrylates (PMCLDA) were cured by UV light to produce polyester elastomers without the use of solvents or heating. Moreover, the crosslinked PMCL elastomers exhibited relatively high elastic moduli, strength, and elongation at break due to the amorphous nature of PMCL precursors [44].

Herein, we aimed to construct porous scaffolds that can withstand dynamic loading as an implant for soft tissue regeneration. Briefly, amorphous polyesters were prepared using controlled ring-opening polymerization of biomass-derived 4-methyl-ε-caprolactone (MeCL), followed by alkynylation. Correspondingly, porous scaffolds were fabricated by thiol-yne photo-crosslinking via the salt template method. The modulus of the scaffolds could be adjusted by changing the M_n of the precursor. In addition, the mechanical property studies were used to assess the elasticity of the scaffold, and minimally invasive injection was attempted. Furthermore, in vitro cellular assays were conducted to evaluate the cytocompatibility and chondrogenic potential of the scaffolds. Finally, using a rabbit articular cartilage defect model, the regenerative effect of the scaffold for soft tissue was determined.

2. Experimental section

2.1. Materials

The reagents used in the study included 4-Methylcyclohexanone (Aladdin, 98%), m-Chloroperoxybenzoic acid (m-CPBA) (Meryer, 85%), 1,4-Benzenedimethanol (BDM) (TCI, 98%), Tin(II) 2-ethylhexanoate [$Sn(Oct)_2$] (sigma, 92.5–100.0%), Potassium hydroxide (KOH) (Aladdin, 99%), 1,1-Carbonyldiimidazole (CDI) (Adamas, 98%), 3-Butyne-1-ol (Aladdin, 97%), 3,6-Dioxa-1,8-octanedithiol (EDT) (Aladdin, 97%), Ethyl (2,4,6-trimethylbenzoyl) phenylphosphinate (TPO-L) (Aladdin, 98%), poly(ε-caprolactone) (PCL), (Aladdin, average $M_n = 80{,}000$), and lipase (Aladdin, from aspergillus niger, 200 U mg^{-1}). All chemicals, unless mentioned otherwise, were used without further purification.

2.2. Synthesis of 4-methyl-ε-caprolactone (MeCL)

The monomer was synthesized via Baeyer-Villiger oxidation of 4-methylcyclohexanone [45]. A constant pressure titration funnel was filled with 120.000 g (1.071 mol, 1 eq) of 4-methylcyclohexanone, which was then diluted with 200 mL of dichloromethane. An additional 239.224 g (1.178 mol, 1.1 eq) of m-CPBA was added to a round-bottom flask and dissolved in 1000 mL of dichloromethane. It was then added dropwise at a rate of 2 drops/s under an ice water bath. The ice water bath was then removed, and the reaction was conducted at 20 °C for 24 h. After the reaction was completed, the solids were extracted by suction filtration and washed three times with saturated sodium thiosulfate, sodium bicarbonate, and sodium chloride aqueous solutions, respectively, to obtain a dichloromethane solution of the crude product. The solution was dried overnight, and 10 g anhydrous magnesium sulfate was added to the as-obtained dry solution. By removing anhydrous magnesium sulfate solids via suction filtration and dichloromethane via rotary evaporation, a crude product was obtained. Subsequently, 1 g of GaH_2 was added to the crude product, which was then sealed and stirred for 10 h. Finally, MeCL was obtained by vacuum distillation (Yield: 90%).

2.3. Synthesis of poly(4-methyl-ε-caprolactone) diol (PMCL-DO)

PMCL-DO was synthesized via ring-opening polymerization, in accordance with reports published previously [44]. As an example of a polymer with a degree of polymerization of 10, 50.000 g (391 mmol, 1 eq) MeCL and 5.391 g (39.1 mmol, 0.1 eq) BDM were added to a flask and vacuum-dried at 55 °C for 3 h. Subsequently, 0.250 g $Sn(Oct)_2$ (0.5% w/w of MeCL) was added via a syringe to the flask as a catalyst under an argon atmosphere. The reaction was conducted at 120 °C under argon for 24 h. The reaction was terminated by dilution with 10 mL dichloromethane, after which PMCL-DO was precipitated in cold petroleum ether and dried under vacuum (Yield: 90%).

2.4. Synthesis of poly(4-methyl-ε-caprolactone) dicarbonylimidazole (PMCL-DC)

The synthesis process of PMCL-DC was referenced from previous literature [36]. Accordingly, 40.000 g PMCL-DO (28.2 mmol, 1 eq) was dissolved in dry toluene (400 mL) before the addition of 13.718 g CDI (84.6 mmol, 3 eq) and 0.200 g KOH (0.5% w/w of polymer) and 24 h of stirring at 60 °C. The mixture was diluted with dichloromethane (600 mL) and washed with deionized water so that the two phases could be distinguished. The solvent was then extracted via rotary evaporation, and PMCL-DC was obtained via precipitation with cold petroleum ether and vacuum drying (Yield: 85%).

2.5. Synthesis of poly(4-methyl-ε-caprolactone) dialkynylate (PMCL-DY)

30.000 g PMCL-DC (18.8 mmol, 1eq) was dissolved in dry toluene (300 mL) before the addition of 3.948 g 3-Butyne-1-ol (56.4 mmol, 3eq) and 0.150 g KOH (0.5% w/w of polymer) and 24 h of stirring at 60 °C. The mixture was diluted with dichloromethane (450 mL) and washed with deionized water in order to separate the two phases. The solvent was removed by rotary evaporation and PMCL-DY was obtained by precipitation with cold petroleum ether and vacuum drying (Yield: 90%).

2.6. Preparation of photocuring mixture

A photocurable mixture comprising the precursor (PMCL-DY), the crosslinker (EDT, with a thiol-to-yne molar ratio of 2:1), and the photoinitiator TPO-L (0.5% w/w). PMCL10-DY photocuring mixture is a typical example. The photocuring mixture comprised 10.000 g PMCL10-DY (6.25 mmol, 1 eq), 2.279 g EDT (12.5 mmol, 2 eq), and 0.061 g TPO-L (0.5% w/w), which were thoroughly mixed by ultrasonic and shaking, stored in a brown bottle at room temperature, and protected from light.

2.7. Preparation of porous scaffold

Porous scaffolds were created using the salt template method [25]. In brief, the salt particles were ground in a mortar and sieved to obtain salt particles with particle sizes of 75–150 μm, 150–300 μm, and 300–450 μm. The salt particles were then added to a cylindrical Teflon mold with an inner diameter of 10 mm and a depth of 10 mm. The salt template was then obtained by removing the mold after 1 h of wetting in the humidity chamber and 3 h of drying at 100 °C in an oven. Subsequently, the salt template was dripped with 1 mL of a photocurable mixture. The mixture template was then exposed to light with a wavelength of 405 nm and a power density of 10 $mW{\cdot}cm^{-2}$ at a distance of 5 cm for 1 min to complete curing (the sample depth was less than or equal to 10 mm). Soaking the cured template in deionized water for 24 h to remove the salt, replacing the water every 8 h, and then freeze-drying finally yielded the porous polymer scaffold.

2.8. General characterization of polymers

The structure of the polymers was determined using ^1H NMR spectra on a Bruker Avance 400 MHz spectrometer using deuterated chloroform ($CDCl_3$) as the solvent and Fourier transformed infrared (FT-IR) spectra on a Nicolet 6700 spectrometer using the KBr method. The molecular weight (M_n) and molecular-weight dispersity (Đ) of the polymers were determined using a Waters 1515 gel permeation chromatography (GPC) equipped with a Tosoh TSK gel Alpha-2500 and Alpha-3000 column in conjunction with polymethyl methacrylate (PMMA) as the standard, with DMF containing 0.01 M lithium bromide as the eluent at a flow rate of 1 $mL{\cdot}min^{-1}$. The column and detector temperature were 50 °C and 35 °C, respectively, and all samples were at the concentration of 2 $mg{\cdot}min^{-1}$.

2.9. General characterization of porous scaffolds

The morphology of the scaffold was determined using scanning electron microscope (FE-SEM S-3400, Hitachi, Tokyo, Japan) at 15 kV. All samples were brittle-broken with liquid nitrogen and sputtered with gold using a putter coater (Ion Sputter E−1045, Hitachi, Tokyo, Japan) for 80 s. The porosity and pore size distribution were tested by mercury intrusion porosimetry (MIP, AutoPore IV 9500). The sample size comprised a cylinder measuring Φ 10 mm × 10 mm (n = 2). In addition, the thermal properties of scaffolds were determined using differential scanning calorimetry (DSC, modulated 2910) from −75 °C to 100 °C at a rate of 10 $°C{\cdot}min^{-1}$ and thermogravimetric analysis (TGA, TG209F1) from room temperature to 600 °C at a rate of 10 $°C{\cdot}min^{-1}$. The crystallization properties of the scaffolds were also evaluated using an X-Ray diffractometer (XRD, D/MAX2550VB/PC) operating at 50 kV and 1000 mA with a scattering angle (2θ) of 5°–70°.

2.10. Mechanical properties

Dynamic mechanical analysis (DMA) was performed on a NETZSCH Instruments (DMA GABO) in compression mode on cylindrical scaffold with 10 mm diameter and 10 mm height. Heating was controlled under a nitrogen atmosphere, and the samples were equilibrated at the designated temperature for 15 min before testing. The DMA experiments were performed in the temperature range of -80-100 °C under a nitrogen atmosphere. The heating rate was 3 $°C{\cdot}min^{-1}$ and the oscillation strain was 0.1% with a frequency of 1 Hz. In addition, compression testing was measured by using universal mechanical tester (Shanghai Kaiyan KY-250N) equipped with a 250 N load cell was used to conduct compression testing. The samples with a size of Φ 10 mm × 10 mm (n = 3) were tested at various strains from 30% to 90% at a rate of 10 $mm{\cdot}min^{-1}$ and at various compression rates from 5 $mm{\cdot}min^{-1}$ to 500 $mm{\cdot}min^{-1}$ at 70% strain. Subsequently, the cyclic compression test was conducted with a 50% compression strain and a 50 $mm{\cdot}min^{-1}$ compression rate. The Young's modulus was derived from the slope of the linear stress-strain area (10% strain). The compression work W_c denotes the area of the stress-strain curve of loading, which represents the recovery work, where W_r is the area of the stress-strain curve of unloading. Finally, the energy loss coefficient was calculated as $1\text{-}W_r/W_c$ [46].

2.11. In vitro degradation

The scaffolds were degraded in vitro in phosphate buffer saline (PBS, pH = 7.4) with and without enzyme (0.5 $g{\cdot}mL^{-1}$). The sample scaffold was a cylinder with a diameter of 10 mm and a height of 2 mm (~0.1 g per piece). Each sample received 5 mL of PBS or an enzyme-containing PBS solution. The samples were then incubated at 37 °C with a shaking rate of 120 $r{\cdot}min^{-1}$. In order to maintain the lipase concentration, the PBS was changed every week and the enzyme solution was replaced daily. After incubation, samples were collected at a predetermined time, washed with deionized water, freeze-dried, and then the change in dry weight was determined. Porous scaffold PCL prepared in the same manner and subjected to the same degradation conditions served as a control group.

2.12. Cell extraction

Two 3-month-old rats were euthanized by over-injection of anesthetic in order to harvest bone marrow stromal cells (BMSCs). BMSCs were harvested from the middle femur of the as-described rats. After extraction and filtration, the bone marrow suspension was washed with α-MEM medium containing 10% FBS and 1% antibiotics (100 $U{\cdot}mL^{-1}$ penicillin G and 100 $\mu g{\cdot}mL^{-1}$ streptomycin sulfate), transferred to 75 cm^2 polystyrene culture flasks, and cultured at 37 °C in a 5% CO_2 incubator with medium changes every two days. For the in vitro experiments described in this study, BMSCs from passages 3–5 was used.

The BMSC phenotype was ascertained by flow cytometry and tri-lineage differentiation staining. The results were shown in Fig. S1. In addition, the surface markers of the BMSCs were analyzed by flow cytometry. CD29 (99.6%), CD44 (98.3%), and CD90 (99.7%) were expressed on the surface of the cells, whereas CD34 (0.039%), CD44 (0.024%), and CD105 (0.18%) were not detectable. After 14 days of osteogenic differentiation and adipogenic differentiation, as well as 21 days of cartilage differentiation, red calcium deposition (Alizarin Red), lipid droplets (Oil Red-O), and blue chondrocyte spheres (Alcian Blue) were observed, indicating that the cells meet the requirements for bone marrow mesenchymal stem cells.

2.13. Cell proliferation

To examine the cell viability of the scaffolds, the proliferation of BMSCs on the scaffolds was evaluated using a cell viability assay (CCK-8). The porous scaffolds prepared from salt sizes range of 75–150 μm were sliced (each slice had a 10.0 mm diameter and a 2 mm thickness with a mass of approximately 100 mg) and placed in 48-well plates with a density of 2×10^4 BMSCs per scaffold. PCL porous scaffolds seeded with the same cell density served as the control group. At 1, 3, and 7 days, CCK-8 was added to each well plate according to reagent: medium = 1:9, and the plates were incubated at 37 °C for 2 h. Subsequently, 100 μl of liquid from each well was added to a clean 96-well plate, and the absorbance at 450 nm on an enzyme marker (Thermo Scientific Multiskan FC) was used to quantify the volume.

2.14. Cell live/dead staining

The activity of BMSCs on scaffolds was evaluated using live/dead fluorescence staining. The porous scaffolds were sliced (10.0 mm diameter, 2 mm thick discs of approximately 100 mg mass each) and placed at a density of 5×10^4 BMSCs per scaffold in 48-well plates (n = 3). The samples were washed 3 times with PBS at 1, 3, and 7 days, respectively. Then, 200 μL of PBS containing cell live/dead fluorescent dye was added to each well (1 mL PBS with 2 μL calcein AM and 3 μL PI), and the staining was incubated for 30 min at 37 °C. Finally, the samples were washed 3 times with PBS and observe using confocal laser-scanning microscopy (CLSM, LEICA TCS-SP8) and to capture images and record the cells.

2.15. Cell morphology on scaffolds

After seeding 2×10^4 cells/scaffold and culturing them for 7 days, the sample was incubated with 2.5% glutaraldehyde for 4 h, washed three times in PBS, and then dehydrated with a series of ethanol concentration gradients (50, 70, 90, 95, 100%). Finally, after being sputter-coated with gold, the morphology of attached cells was observed using a scanning electron microscope (SEM).

2.16. Chondrogenic gene expression

To evaluate the chondrogenic differentiation ability of the scaffolds, PMCL20-DY scaffolds prepared from salt sizes ranging from 75 to 150 μm were placed at the bottom of a 48-well plate (10 mm diameter, 2 mm thickness, 100 mg per piece), and each scaffold was seeded with (5×10^4) BMSCs and cultured in a common medium (DMEM culture medium supplemented with 10% FBS and 1% antibiotics). PCL porous scaffolds seeded with the same cell density served as the control group. Utilizing the Trizol reagent (TIANGEN) and reverse transcriptase (Hifair), complementary DNA (cDNA) was synthesized from extracted RNA. Subsequently, Chondrogenic gene expression of Aggrecan, COL II, and SOX9 at 7 and 14 days was evaluated using real-time PCR, with GAPDH serving as an internal control gene. Finally, the relative expression of each gene relative to the control gene was determined. Each experiment was conducted three times. The primer sequences used are listed in Table S1 of the supporting information.

2.17. Immunofluorescence staining

Immunofluorescence staining experiments were performed in order to observe the chondrogenic differentiation of cells on scaffolds. Scaffolds, prepared from a salt size range of 75–150 μm, were placed at the bottom of 48-well plates (10 mm diameter, 2 mm thickness approximately 100 mg per piece), and each scaffold was inoculated with (5×10^4) BMSCs and cultured in normal medium (DMEM culture medium supplemented with 10% FBS and 1% antibiotics). After 14 days of culture, the cells were washed three times with PBS and fixed at room temperature for 15 min with 4% paraformaldehyde. Subsequently, immunofluorescence staining was performed for the nucleus, cytoskeleton, and COLII. Following an overnight incubation at 4 °C with anti-COL II primary antibody (1:200), cells were incubated with Alexa Fluor 488-labeled secondary antibody (1:200) for 1 h. Cells were stained with TRITC Phalloidin (1:200) for 40 min in a 37 °C incubator and DAPI (1:200) for 10 min at room temperature, and then washed three times with PBS before confocal laser-scanning microscopy (CLSM, LEICA TCS SP8) was used to observe and photograph the staining.

2.18. Animal experiments

Three-month-old New Zealand White rabbits (2.5–3 kg, Experimental Animal Center, Shanghai Jiao Tong University School of Medicine Affiliated Ninth People's Hospital) were randomly divided into three groups (n = 4 joints): blank control, PCL, PMCL20-DY. The rabbits were placed supine under general anesthesia, and the knee was exposed by a parapatellar medial incision. The patella was dislocated to fully expose the distal articular surface of the femur. Susbequently, a cylindrical drill was used to create an osteochondral defect (5 mm in diameter and 4 mm in depth) on the articular surface of the femoral patellofemoral groove. After flushing the joint with sterile isotonic saline, the defect was implanted with a PCL scaffold, a PMCL20-DY scaffold. The defect was left unfilled as a blank control group. Layer by layer, the knee capsule was sutured to the skin, and the wound was closed. After surgery, the animals were allowed to move freely in their cage. Finally, at 12 weeks, the animals were euthanized by over-anesthesia, and regenerative histological samples were collected for further analysis. All experimental procedures were approved by the Experimental Animal Ethics Committee of Shanghai Jiao Tong University School of Medicine Affiliated Ninth People's Hospital (SH9H-2022-AB17-SB) and strictly adhered to its rules and regulations.

2.19. Histological staining

The samples were first fixed with 4% paraformaldehyde for 3 days, followed by decalcification with 10% EDTA, dehydration with graded ethanol, cleaning with xylene, embedding in paraffin wax, and slicing into 4 μm thick slices. To visualize the cartilage matrix, the sample was stained with Safranin-O and fast green. Histomorphometric analysis was performed on areas of the defects that were positively stained with Safranin-O. Masson trichrome and hematoxylin/eosin (H&E) stains were also used as references for histological analysis. All stained samples were observed and analyzed under a fluorescent inverted microscope.

2.20. Immunohistochemical staining

In order to extract antigen for immunohistochemical staining, samples were dewaxed and incubated for 1 h at 37 °C with 0.4% pepsin (Roche). The samples were blocked for 0.5 h in 10% blocking serum. Following an overnight incubation with murine primary antibodies COL I, COL II, and COLX (Abcam, Cambridge, UK), they were incubated for 1 h with secondary antibodies. After incubation with 3,3′-diaminobenzidine (DAB) for color development, the samples were

counterstained and fixed with hematoxylin.

3. Results and discussion

3.1. Synthesis, characterization and cross-linking of PMCL-DY precursor

Fig. 1a depicts the precursor synthesis pathway for poly(4-methyl-ε-caprolactone) dialkynylate (PMCL-DY). Poly(4-methyl-ε-caprolactone) diol (PMCL-DO) was produced via ring-opening polymerization (ROP) of the monomer 4-methyl-ε-caprolactone (MeCL) with 1,4-benzenedimethanol (BDM) as the initiator and $Sn(Oct)_2$ as the catalyst. The hydroxyl group at the end of PMCL-DO was then reacted with 1,1-carbonyldiimidazole (CDI) to produce the active imidazole-capped poly (4-methyl-ε-caprolactone) dicarbonylimidazole (PMCL-DC). In the final step, PMCL-DC was reacted with 3-butyne-1-ol to produce dialkynylated PMCL-DY precursor. ^{1}H NMR and FT-IR were utilized to characterize the molecular structure of PMCL-DY, the final product, as well as intermediates PMCL-DO and PMCL-DC. Fig. S2 (Supporting Information) depicts the typical ^{1}H NMR spectra of PMCL-DO, PMCL-DC, and PMCL-DY with a monomer-to-initiator feed ratio of 10:1. At 0.94 ppm, 2.33 ppm, and 4.12 ppm, the corresponding signal peaks of PMCL-DO polymer were measured. CDI modification resulted in the appearance of three peaks of imidazole at 8.15 ppm, 7.44 ppm, and 7.09 ppm relative to the ^{1}H NMR spectra of PMCL-DO and PMCL-DC. The complete disappearance of the methylene proton signal adjacent to the terminal hydroxyl group at 3.69 ppm indicates the complete conversion of all terminal hydroxyl groups to imidazole groups. In addition, the imidazole peaks disappeared completely and the new signal peaks of alkynyl groups at 4.23 ppm, 2.58 ppm, and 2.03 ppm appeared after alkynylation. It was determined that imidazole groups were entirely reacted and that alkynyl groups were successfully modified at the end of PMCL. In comparison to the FT-IR spectra of PMCL-DO, PMCL-DC, and PMCL-DY (Fig. S3, Supporting Information), the peak of the hydroxyl group at 3400-3600 cm^{-1} disappeared with the modification of CDI and was followed by the appearance of the imidazole peak at 1000 cm^{-1} and 3000 cm^{-1}. It was suggested that the imidazole group reacted effectively. After alkynylation, the imidazole group's peak disappeared and the alkynyl group's peak appeared at 3300 cm^{-1}, demonstrating that the imidazole group was completely replaced by the alkynyl group. In addition, the GPC curves of PMCL-DO, PMCL-DC, and PMCL-DY exhibited unimodal peaks with low molecular-weight dispersities (Đ) of 1.22, 1.25, and 1.30, respectively (Fig. S4, Supporting Information). Thus, it was established that PMCL had been successfully end-capped with alkyne groups.

Preparation of a series of PMCL-DYs with theoretical degrees of polymerization (DP) of 10, 20, 50, and 100 is summarized in Table S2 of the Supporting Information. The M_n of PMCL-DYs calculated by ^{1}H NMR (Fig. S5, Supporting Information) were close to the theoretical values, indicating that the designed degree of polymerization was nearly identical to the degree of polymerization observed in the final product. Meanwhile, the GPC curves exhibited unimodal peaks (Fig. S6, Supporting Information), and the relative M_n (PMMA standard) was close to its theoretical values with a Đ value below 1.5. It has been demonstrated that PMCL-DYs with a modifiable DP can be obtained through controlled

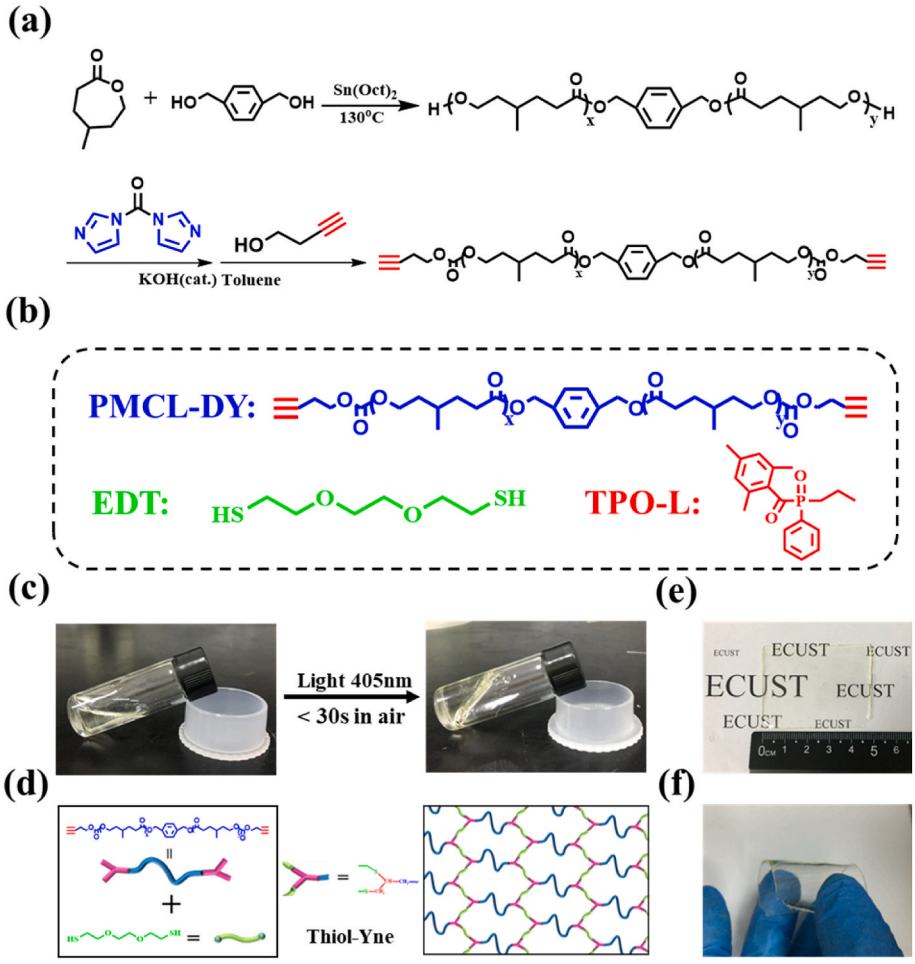

Fig. 1. (a) Synthesis routes of the PMCL-DY precursors. (b) Composition of the photocuring mixture. (c) Photographs of the cross-linking photocuring mixture and (d) schematic illustration of the cross-linking network. Photographs of (e) light transmission and (f) flexibility of films.

ROP and end-group modification. Notably, the entire reaction was conducted under mild conditions. The intermediate and final production purification processes were simple and highly efficient. Therefore, it is advantageous to increase precursor production.

The liquid precursor PMCL-DY, cross-linker 3,6-dioxa-1,8-octanedithiol (EDT), and photoinitiator ethyl (2,4,6-trimethylbenzoyl) phenylphosphinate (TPO-L) were forming a photocuring mixture for thiol-yne photo-crosslinking (Fig. 1b). In the mixture, the ratio of thiol to yne was 2:1, which is the theoretical ratio of complete cross-linking between thiol and yne. Notably, polymers with a DP of 100 have too few cross-linking points to be cured; consequently, only polymers with DP of 10, 20, and 50 were studied. As shown in Fig. 1c, the liquid mixture cured in 30 s when irradiated at a visible wavelength of 405 nm in air. The conversion of polyester alkyne groups before and after cross-linking was measured by FT-IR, and the results are displayed in Fig. S7 of the Supporting Information. The disappearance of the alkyne group peak at 3300 cm^{-1} after 30 s of irradiation indicates that thiol-yne has been completely cross-linked. According to the step-growth polymerization mechanism of thiol-yne click chemistry, Fig. 1d depicts the ideal schematic diagram of the regular network formed after cross-linking [47,48]. Further, the mixture was molded into a rectangular piece with dimensions of 5 cm × 4 cm × 2 mm; the resulting product was highly transparent (Fig. 1e) and flexible (Fig. 1f) with no uncrosslinked residue on the surface. Notably, the cross-linking procedure could be carried out in ambient air and at room temperature. The thiol-yne reaction is less susceptible to oxygen inhibition than other photoinitiated reactions [49]. Thus, thiol-yne reactions can polymerize rapidly at lower concentrations of photoinitiators and in air environments, which may increase the number of available processing technologies. In particular, the oxygen tolerance of thiol-yne reactions renders them highly cytocompatible, as they do not generate intracellular reactive oxygen species (ROS) as is commonly observed during free radical polymerization [50,51]. Meanwhile, the platform effect of click chemistry for the loading of active ingredients has been reported. Moroni et al. [35], loaded vascular endothelial growth factor mimetic peptides onto PCL diacrylate electrospun vascular scaffolds using a thiol-ene reaction, which effectively stimulated in vivo angiogenesis. These benefits of the thiol-yne reaction make the material more suitable for use in tissue engineering.

3.2. The fabrication and thermal properties of porous scaffolds

Fig. 2a depicts the preparation of porous scaffolds using the salt template method. The pre-formulated photocuring mixture was added drop by drop to the salt template, which was then exposed to 405 nm light and cured, followed by soaking in deionized water and freeze-drying. The liquid photocuring mixture at room temperature was cross-linked after penetrating the salt template in the absence of an organic solvent. As shown in Fig. 2b, various sized and geometrically shaped porous scaffolds were created. Such complex geometric scaffolds could be easily modified by altering the mold's shape. During the pore-making procedure, sieves with pore size distributions of 75–150 μm, 150–300 μm, and 300–450 μm were used to screen the salt particles. Fig. 2c–e depict SEM images of the cross-sectional morphologies of these scaffolds. It was discovered that the pores are interconnected and that the pore size increases significantly as the salt size rises. The pore sizes were counted in the histogram and showed a uniform and normal distribution. The main pore sizes of the scaffolds were generally distributed between 75–150 μm, 100–300 μm and 150–400 μm, respectively. The statistical mean pore sizes of the scaffolds were 99.4 ± 64.5 μm, 173.2 ± 99.3 μm and 234.5 ± 143.6 μm, which corresponded to the salt size of the templates. It seemed that the prepared pore distribution by salt template was predictable and reproducible. Subsequently, the porosity and pore size distribution were tested by mercury intrusion porosimetry (MIP). The porosity of the three scaffolds with different pore sizes was 69.6 ± 1.5%, 67.9 ± 2.1% and 63.8 ± 1.2%, respectively, indicating that the porosity decreased with increasing salt size. Thus, it was further confirmed that the pores were interconnected. The pore size distribution is shown in Fig. 2f–h. As evident from the graph, pores of the scaffolds were found to have a normal distribution, with median pore sizes of 60.30 μm, 72.36 μm and 89.60 μm, respectively. Additionally, it was in agreement with the SEM images, indicating that the pore size increased with increasing salt size. However, MIP demonstrated that the porosity and pore size distribution of the scaffolds were slightly modifiable by slat size, which significantly contradicts the SEM image analysis results. This may be attributed to the various characterization principles and techniques. In the mercury intrusion test, Hg was forced into scaffolds by pressure, which may have led to the deformation of pores with elastic modules of a few kPa. Therefore, the liquid precursor greatly simplified the fabrication process with eco-friendly, avoiding the use of organic solvents and the possibility of cytotoxicity. The interconnected micron-scale pores facilitate nutrient transport and metabolite release during subsequent cell culture [52,53].

The precursors of PMCL-DY with DP of 10, 20, and 50 were fabricated into porous scaffolds using salt templating and were named PMCL10-DY, PMCL20-DY, and PMCL50-DY, respectively. As illustrated in Fig. 2i, the three scaffolds demonstrated a white porous sponge-like with similar appearance, indicating that variations in the M_n of precursor did not significantly alter the porous properties of the scaffolds. The secondary heating DSC curves of the three scaffolds are shown in Fig. 2j. The scaffolds displayed a shallow glass transition slope from a glassy to a rubbery state at −46.1 °C, −54.0 °C, and −58.1 °C, respectively. The T_g of uncrosslinked polymers with DP 10, 20, and 50 was −58.5 °C, −59.7 °C, and −60.8 °C, respectively (Fig. S8, Supporting Information), which was significantly lower than the scaffolds. Thus, it was hinted that cross-linking impeded the movement of polymer chain segments, resulting in a rise in T_g. In addition, PMCL10-DY exhibited the greatest difference in T_g before and after cross-linking, caused by the greatest degree of cross-linking. Subsequently, TGA was used to investigate the thermal decomposition properties of scaffolds. As shown in Fig. 2k, the onset decomposition temperature (T_d) increased as the DP of the precursor increased, from 215.4 °C for PMCL10-DY to 246.8 °C for PMCL50-DY. The differentiation curves (Fig. S9) clearly demonstrated the weight loss rate variations of each component in the scaffolds. It was revealed that the crosslinker EDT decomposed at a lower temperature than PMCL. In general, the T_d of all scaffolds was above 200 °C, indicating that scaffolds have good thermal stability. In addition, XRD was utilized to examine the crystallization properties of the scaffolds. As illustrated in Fig. S10, the XRD curves of three scaffolds exhibited broad-wrapped peaks, indicating that scaffolds with 10, 20, and 50 DP were completely amorphous after cross-linking.

3.3. Mechanical properties of the scaffolds

The scaffolds were subjected to dynamic mechanical analysis (DMA), and the storage (E′) and loss moduli (E″) were monitored in a compression mode as a function of temperature from −80 to 100 °C (Figs. S11–S13). It was demonstrated that the T_g of the scaffolds was −32.5 °C, −38.5 °C, and −44.1 °C, which was consistent with the trend of DSC. Deviations in the values may be caused by variations in the testing machines and heating rates. Throughout the entire temperature range, with the exception of the glass transition, the E′ was greater than the E″, providing additional evidence that the scaffolds were chemically cross-linked. In the rubbery region of the scaffolds, the modulus E′ was found to be 0.122 MPa, 0.052 MPa and 0.012 MPa, thus, decreasing with increasing DP of precursors (Fig. 3a). The increase of M_n could have resulted in a reduction in crosslink density and modulus of the scaffold. For all scaffolds, the rubbery plateau moduli were relatively constant throughout the temperature sweep, which indicated that the mechanical integrity of the network was maintained.

The effect of different porosity on the modulus of scaffolds was examined. The scaffolds prepared by salt sizes ranging from 75–150 μm, 150–300 μm and 300–450 μm with DP 10 of precursor were given the

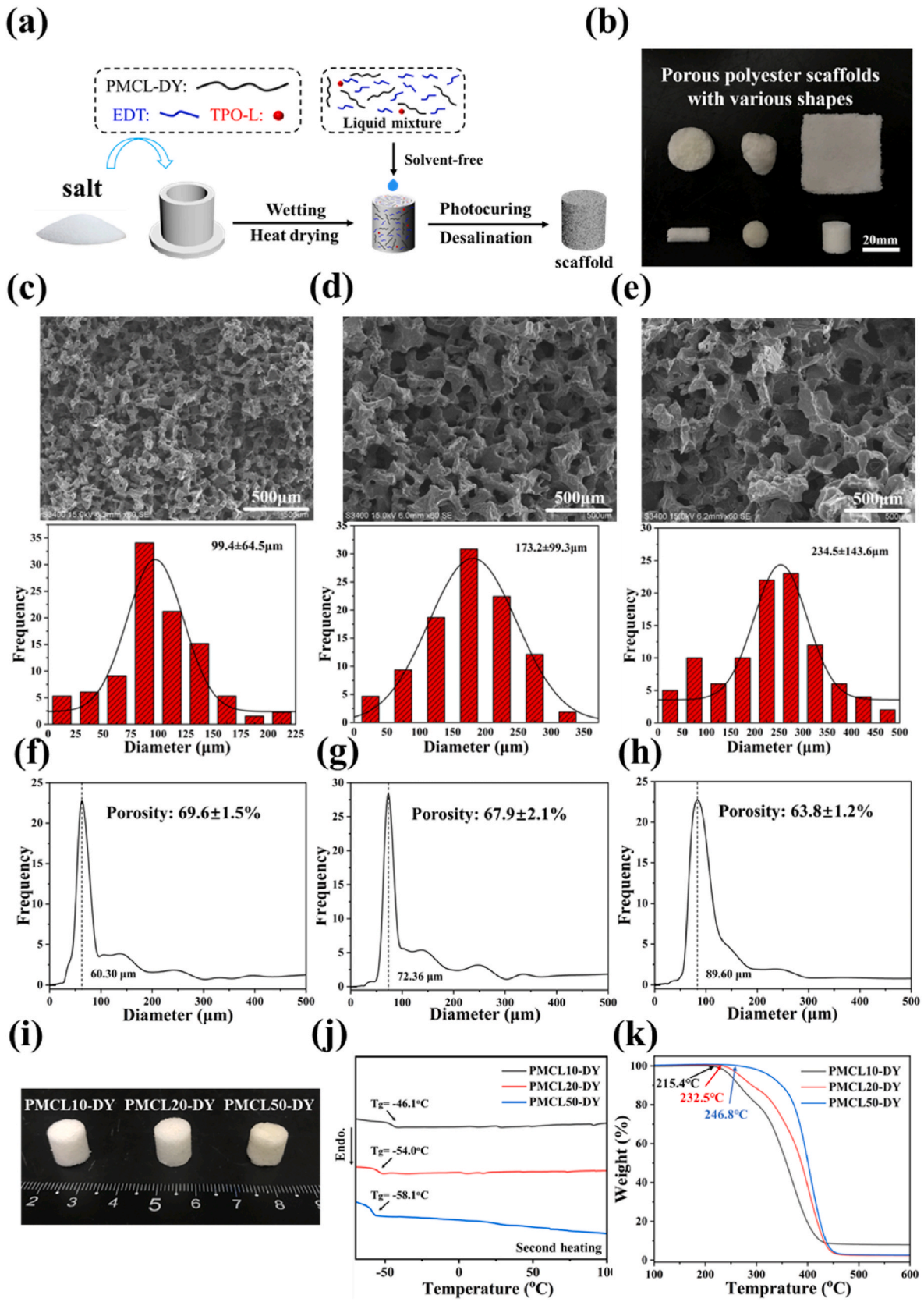

Fig. 2. (a) Preparation route of porous scaffolds. (b) Macroscopic photographs of various 3D shaped porous scaffolds. (c–e) SEM images of cross-sectional morphologies and (f–h) pore size distribution and porosity of different pore size scaffolds. (i) Macroscopic photographs, (j) DSC secondary heating curve and (k) TGA curves of scaffolds PMCL10-DY, PMCL20-DY and PMCL50-DY.

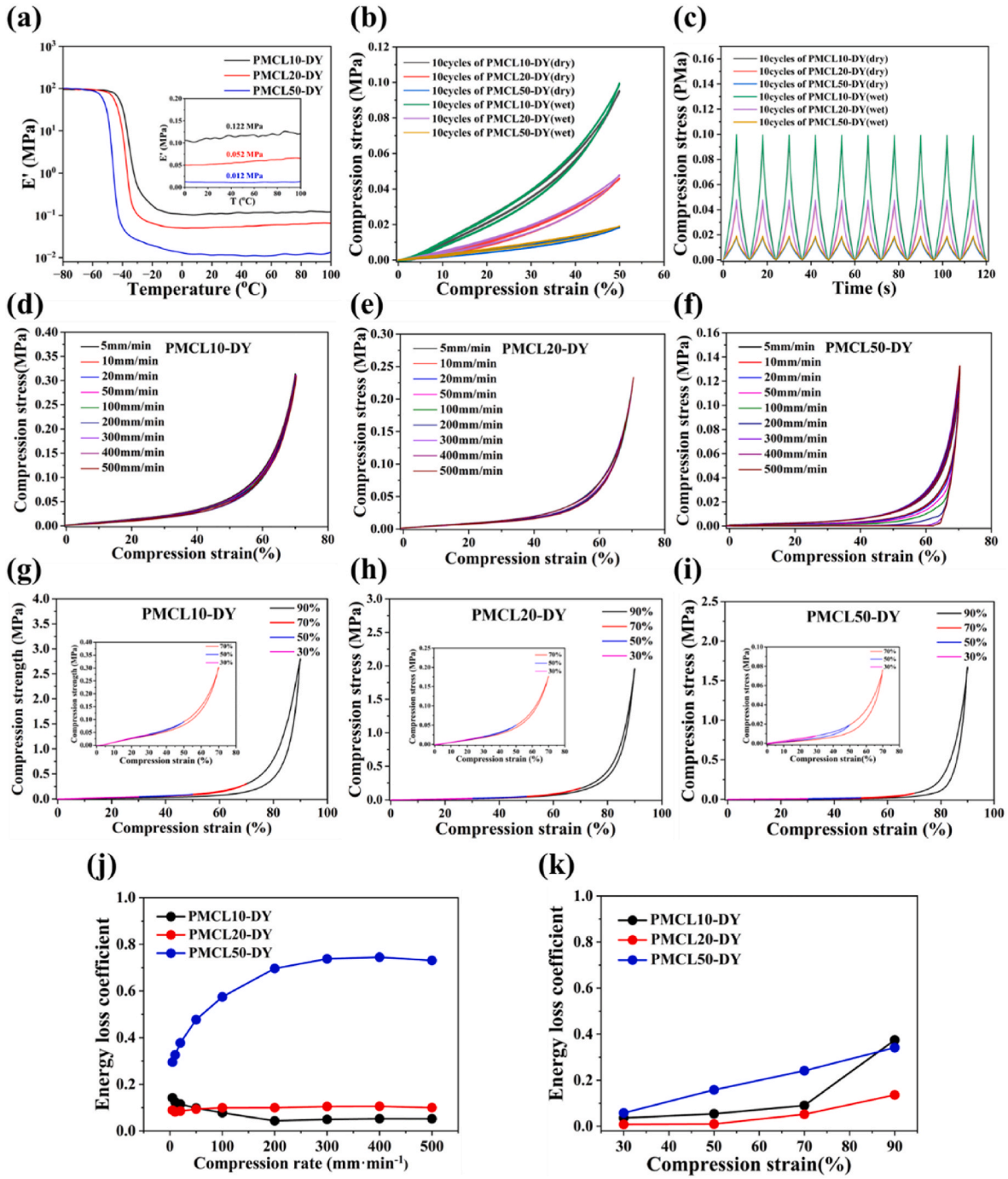

Fig. 3. (a) Overlay of the storage modulus curves of scaffolds PMCL10-DY, PMCL20-DY and PMCL50-DY. (b) 10 cycles compression stress-strain curve and (c) stress-time curve of scaffolds PMCL10-DY, PMCL20-DY and PMCL50-DY in dry and wet states. Stress-strain curves of (d) PMCL10-DY, (e) PMCL20-DY, and (f) PMCL50-DY scaffolds with compression rates in the range of 5–500 mm min^{-1}. Stress-strain curves of (g) PMCL10-DY, (h) PMCL20-DY, and (i) PMCL50-DY scaffolds with compression strains of 30–90%. (j) Energy loss coefficients for compression rates of 5–500 mm min^{-1}. (k) Energy loss coefficients for compression strain of 30–90%.

designations PMCL10-DY (75–150), PMCL10-DY (150–300), and PMCL10-DY (300–450). The compressive stress-strain curves of the scaffolds at 70% strain are shown in Fig. S14. In addition, the modulus and porosity are summarized in Table S3. As observed, the modulus of the scaffolds did not differ significantly from one another. It could be attributed to similar porosity, resulting in similar cross-sectional filling densities of materials. Furthermore, cyclic compression of the scaffolds was characterized. The cyclic compression properties of dry and wet scaffolds (soaked for 24 h in PBS) were examined. Before and after soaking, the dimensions of the scaffolds did not change significantly (Fig. S15). Cyclic compression stress-strain curves (Fig. 3b) revealed that all scaffolds exhibited nonlinear characteristics accompanied by slight hysteresis during loading and recovery. In addition, Fig. 3c depicts the stress-time curves for the 10 cycles of scaffolds, revealing that the peak patterns were nearly identical for each cycle. Both dry and wet scaffolds were found to be elastic and capable of recovering well from dynamic cycling. Table S4 summarizes the quantitative calculations of the modulus, maximum stress (50% strain), and energy loss coefficients of scaffolds. The compressive modulus of the dry scaffolds PMCL10-DY, PMCL20-DY, and PMCL50-DY was determined to be 115.4 ± 10.3

kPa, 54.5 ± 3.7 kPa, and 9.5 ± 0.6 kPa, respectively. All scaffolds had moduli in the range from 9.5 to 115.4 kPa, which was in good agreement with the results obtained via DMA. The modulus of the wet scaffolds PMCL10-DY, PMCL20-DY, and PMCL50-DY increased slightly when compared to the dry scaffolds: 122.8 ± 17.7 kPa, 57.4 ± 8.5 kPa and 11.8 ± 1.5 kPa, respectively. In addition, there was a slight increase in the maximum stress and energy loss coefficient between the wet and dry scaffolds. It may be due to the buffering effect of water within the scaffold. Thus, it was demonstrated that scaffolds maintained consistent mechanical properties under both dry and physiological conditions, which is advantageous for tissue engineering. In subsequent tests, dry scaffolds were utilized to eliminate the influence of water within the scaffold. Notably, the energy loss coefficient of the scaffolds was lower than those of aerogel elastomers [54–56], hydrogels [57–59], and other elastomers [60–62]. Thus, a lower energy loss coefficient would enhance the fatigue resistance of the scaffold, which is necessary for the cyclic properties of soft tissue physiological loading [46].

To demonstrate the elasticity of the scaffold in greater detail, it was subjected to various compression rates and strains. The recovery performance of three scaffolds was evaluated by increasing the compression rate from 5 to 500 mm·min^{-1} at 70% strain; the results are depicted in Fig. 3d–f. When the test rate exceeded 50 mm·min^{-1}, PMCL50-DY's recovery rate became inconsistent with the preset rate as the test rate increased. While the PMCL10-DY and PMCL20-DY recovery rates could be consistent at all rates. In Table S5 and Fig. 3j, the energy loss coefficients at each rate for the three scaffolds were quantified in greater detail. With increasing test rate, the energy loss coefficients of PMCL50-DY increased from 0.3 to 0.7. When the set rate exceeded 50 mm·min^{-1}, PMCL10-DY had lower energy loss coefficients than PMCL20-DY. In general, scaffolds with a higher M_n precursor exhibited a greater energy loss coefficient, probably because a looser network was not easy to be recovered.

Furthermore, the compression strains (30–90%) of three scaffolds were evaluated in Fig. 3g–i. Below 70% compressive strain, the stress-strain curves of PMCL10-DY exhibited a slight hysteresis. When the compressive strain reached 90%, the stress-strain curve appeared a large hysteresis due to the damage of the scaffold. By increasing the compression strain, the hysteresis in the stress-strain curves of PMCL50-DY grew steadily larger. It was worth noting that the stress-strain curves of the PMCL20-DY scaffold maintained a slight hysteresis at 30%-90% compressive strain. In addition, the energy loss coefficient at 30%–90% compressive strain of the three scaffolds was quantified, and the result is summarized in Table S5 and depicted in Fig. 3k. As strain increased, the energy loss coefficient of PMCL10-DY scaffolds rose from 0.04 to 0.4, the energy loss coefficient of PMCL50-DY scaffolds rose from 0.06 to 0.36. In contrast, PMCL20-DY maintained an energy loss coefficient below 0.15. The PMCL20-DY, thus, exhibited excellent elastic performance under all conditions, which was expected to meet the frequency range of human walking (0.6–2 Hz) and the amplitude of strenuous exercise, based on testing at different rates (0.006–0.6 Hz) and strains (30–90%) [46].

3.4. Fatigue resistance and minimally invasive injection of PMCL20-DY scaffolds

In order to further examine the elasticity of the PMCL20-DY scaffold, its fatigue resistance was evaluated. As shown in Fig. 4a, after 10,000 cycles of compression with a compression strain of 70%, the stress-strain curve of the scaffold had no significant decay. The modulus, maximum stress, and the energy loss coefficient are summarized in Table S6. Quantitative analysis revealed that the scaffolds maintained low energy

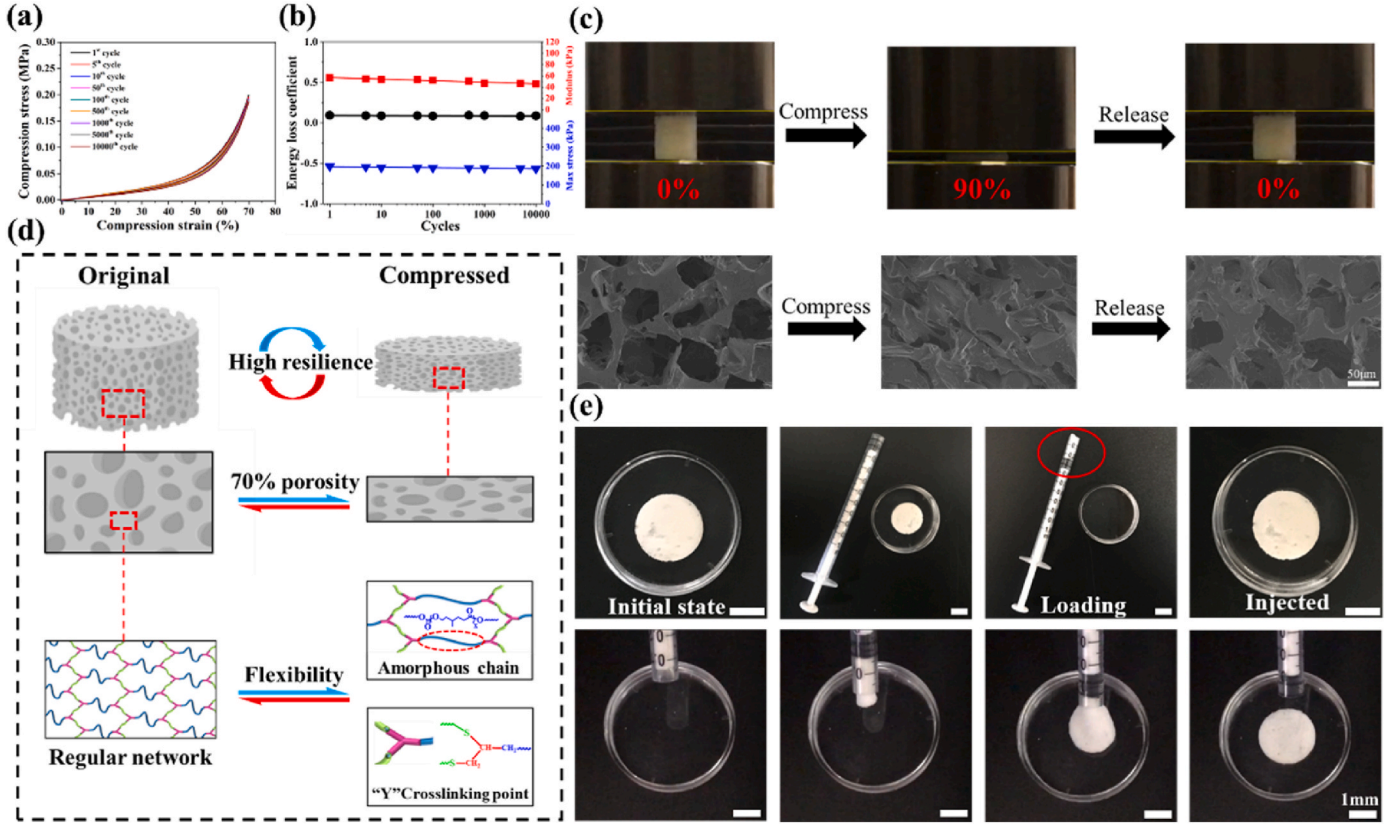

Fig. 4. (a) Stress-strain curve of PMCL20-DY scaffold under 10,000 cycles of compression at strain of 70%. (b) Energy storage modulus, energy loss coefficient and maximum stress change of PMCL20-DY scaffold under 10,000 cycles of compression. (c) Macroscopic and microstructural changes during compression (strain = 90%) and shape recovery of PMCL20-DY scaffold. (d) Schematic of the scaffold's superior performance mechanism. (e) Images of porous scaffolds reloaded as syringes and injected from syringes.

loss coefficients (<0.1) throughout the test, and that there was no significant decrease in maximum stress (>90%) or modulus (>80%) (Fig. 4b). The compression recovery process of the PMCL20-DY scaffold at 90% strain was monitored, and the results are depicted in Movie S1 in the Supporting Information. Fig. 4c displays the images of the beginning of compression at 90% strain and the end of compression. It was observed that after 90% compression, the scaffold could be returned to its original height with almost no change in shape. The pore morphology of the scaffold during compression was also characterized using SEM. During the compression process, the pores changed from an open state to a completely squeezed state. Upon releasing the pressure, the pores were able to return to an open state without structural damage, demonstrating the excellent elasticity and dynamic flexibility of the scaffold. The possible mechanism for the high resilience and excellent fatigue resistance of the scaffold is proposed in Fig. 4d. Macroscopically, the scaffold is composed of an elastic solid matrix and interconnected pores. When compressed, the matrix undergoes elastic deformation preferentially and squeezes the surrounding pores. The presence of approximately 70% porosity may have contributed to the majority of volume change during deformation. From a microscopic perspective of the solid matrix formed by the crosslinking of thiol-yne, the scaffold matrix is flexible due to the synergistic effect of amorphous precursors and “Y" crosslinking points. For comparison, free radical polymerization produces a non-uniform network, which led to inconsistency between the overall and local mechanical properties [37]. A regular network was formed during thiol-yne crosslinking by orthogonal step-growth polymerization. Thus, it is possible that fewer spatial and topological defects resulted in a more uniform distribution of stresses during deformation, thereby reducing fatigue sensitivity.

Moreover, both clinical treatments and tissue-engineered scaffold implantation are invasive, thereby increasing surgical risk and postoperative recovery time for patients. Minimally invasive treatments are increasingly utilized in clinical procedures to reduce the risk of infection, the size of the incision, and the patient’s recovery time [63]. Due to the scaffold’s pliability and high resiliency (90% compression strain with full recovery), minimally invasive injections were attempted, and the scaffold was placed in a syringe for injection. As depicted in Fig. 4e, the PMCL20-DY porous scaffold (Ø 2 cm × 2 mm) could be curled and inserted into a 1 mL syringe before being released. After injection, the scaffold could instantly revert to its original form and remain stable. The injection process is depicted in Movie S2 in the Supporting Information. Currently, minimally invasive therapeutic polymer materials are dominated by hydrogels and shape memory materials [64,65]. However, hydrogels and shape-memory materials have a difficult time withstanding dynamic cycling and providing dynamic support for defects [66]. Therefore, the PMCL20-DY scaffold was compressible for minimally invasive treatment and provided dynamic support to the tissue after implantation, demonstrating great potential as a soft tissue replacement graft scaffold for minimally invasive surgery.

3.5. *In vitro degradation, cell proliferation and differentiation assay of PMCL20-DY scaffolds*

To investigate scaffold degradation, PMCL20-DY porous scaffolds were subjected to degradation experiments in PBS solution, either with or without an enzyme. The porous PCL scaffold prepared using a salt template was used as a comparison. After 12 weeks of PMCL20-DY and PCL scaffold degradation in PBS, the residual mass ratio was found to be 80.3 ± 3.9% and 95.8 ± 1.6%, respectively (Fig. S16, Supporting Information). The degradation profiles of PMCL20-DY and PCL scaffold in enzyme solution are shown in Fig. S17. As observed, after 14 days of degradation in enzyme solution, the residual mass ratio of the PMCL20-DY scaffold was 14.4 ± 9.0%, while the residual mass ratio of the PCL scaffold was 71.0 ± 9.7%. The PMCL20-DY scaffold degraded significantly faster than the PCL scaffold, particularly in enzyme-containing PBS solutions. It has been reported that the amorphous region of polymers is more susceptible to chain hydrolysis than the crystalline region [67]. Therefore, completely amorphous PMCL20-DY scaffolds were more susceptible to hydrolysis than semicrystalline PCL scaffolds. In addition, the ether bonds of the cross-linker in the PMCL20-DY scaffold had a higher affinity for water, thereby facilitating hydrolysis. Thus, it is reasonable to ascertain that PMCL20-DY scaffolds degraded significantly faster than the PCL scaffolds. Due to the presence of cells, lipases, and other natural pathways, the enzymatic degradation results of scaffolds could be better used as a reference for in vivo experiments.

The cytocompatibility of the scaffold was evaluated by proliferation experiments of BMSCs on PMCL20-DY scaffolds. Accordingly, we seeded BMSCs on a 3D porous PMCL20-DY scaffold (Fig. 5a). As depicted in Fig. 5b, the cell live/dead staining results demonstrated significant cell growth with a healthy spindle shape within 7 days on the scaffold and a high cell viability of >95%. CCK-8 was used to quantify cell proliferation (Fig. 5c), and the results demonstrated that the PMCL20-DY scaffold exhibited comparable growth to the PCL scaffold, indicating the good cytocompatibility of the PMCL20-DY scaffold. The PCL-like molecular structure of the PMCL20-DY scaffold may be responsible for its high cytocompatibility. 7 days after being seeded on the porous scaffolds, the SEM image (Fig. 5d) revealed that the cells’ spreading morphology was optimal. The laser confocal image revealed a 3D cell distribution on the porous scaffolds (Fig. 5e), which may be the result of cell migration, infiltration, and growth within the interconnected pores of the scaffold.

To further confirm BMSCs differentiation on PMCL20-DY scaffolds, chondrogenic-related genes were analyzed using quantitative real-time reverse transcription-polymerase chain reaction (qRT-PCR). After 14 days of co-culture of PMCL20-DY scaffold with BMSCs, the expression of chondrogenic-related genes including aggrecan, COL II, and SOX9 was significantly upregulated (Fig. 5f–h). To directly observe the expression of COLII protein in the co-cultured cells, COL II, Nucleus and F-actin were fluorescently marked using immunofluorescence assay. In the fluorescence images (Fig. 5i), the expression of the COLII protein was significantly higher on the PMCL20-DY scaffold than it was on the control. These results indicated that PMCL20-DY scaffolds were capable of promoting the differentiation of BMSCs into cartilage. The ability of aggrecan to bind to hyaluronic acid and chondrocytes stabilizes the fixation of aggrecan on the ECM, which is essential to maintain the unique biomechanical properties of cartilage [25]. COLII represents 90–95% of the collagen in the cartilage matrix and forms fibrils intertwined with aggrecan. SOX9 is a member of the Sry-related high mobility group box (SOX) family of transcription factors and a key transcription factor in cartilage formation, capable of directly regulating the expression of COL II and aggrecans [68]. Therefore, high expression of aggrecan, COLII, and SOX9 mRNA may facilitate cartilage regeneration. The pro-chondrogenic differentiation of PMCL20-DY may be attributable to the scaffolds’ pores, which were appropriately distributed within the range of 75–150 μm. It has been demonstrated in previous studies that the pore size of the scaffold affected cell proliferation and differentiation. The scaffold with pores ranging from 60 to 125 μm was reported to promote stem cell differentiation into cartilage, prevent vascular invasion and endochondral ossification, and preserve the cartilage phenotype [69]. Due to the hydrophobicity and reduced crystallinity of the lateral methyl groups, PMCL films demonstrated superior GAG deposition compared to PCL films in our previous research. Moreover, a softer matrix and a weaker adhesion on the matrix are thought to be more conducive to the formation of cell aggregates, thereby promoting optimal cartilage differentiation [70]. Overall, the appropriate pore size and relatively soft matrix of the scaffold could better mimic the internal environment of cartilage tissues, thereby promoting the upregulation of cartilage-related genes and the expression of COLII protein, indicating that the PMCL20-DY scaffold has a promising potential for pro-chondrogenic differentiation.

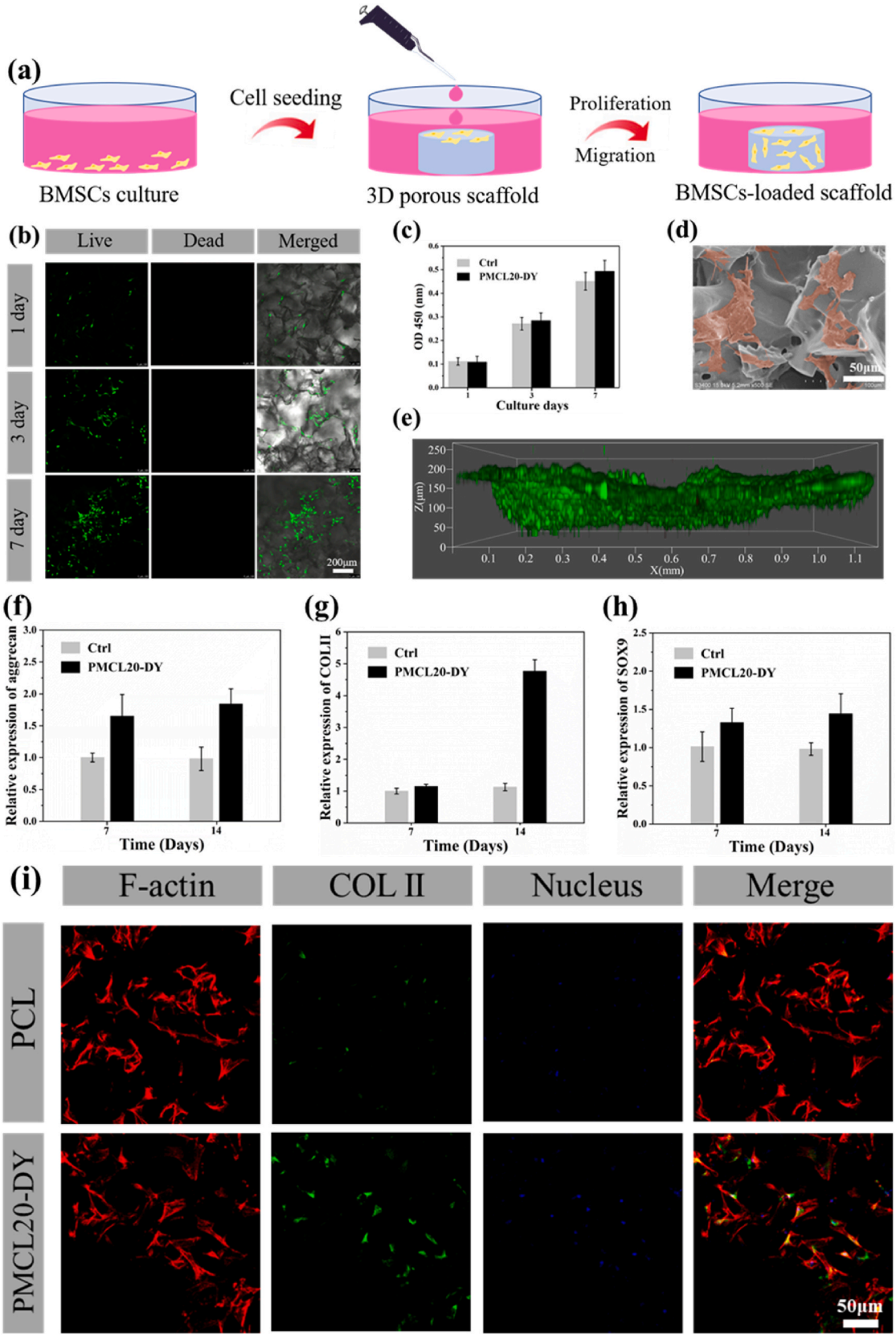

Fig. 5. (a) Schematic of experimental design of the in vitro cell inoculation of the 3D porous scaffold; (b) Live/dead fluorescence staining images of BMSCs cultured on PMCL20-DY porous scaffold for 1, 3, 7 days; (c) Cell viability assay of BMSCs cultured on PMCL20-DY porous scaffold for 1, 3, 7 days; (d) SEM image of cell morphology of BMSCs after 7 days of culture on PMCL20-DY; (e) 3D fluorescence staining images of BMSCs cultured on PMCL20-DY for 7 days; Expression of chondrogenic genes including (f) Aggrecan, (g) Col II and (h) Sox9; (i) Immunofluorescence staining of cell differentiation (multiple cross-sectional stacked views).

3.6. In vivo cartilage regeneration assay of PMCL20-DY scaffold

To demonstrate elastomeric tissue repair under in vivo cyclic loading of PMCL20-DY scaffold, a mature New Zealand white rabbit cartilage repair model was used. The defect created in the center of the talocrural groove was implanted with a porous PMCL20-DY scaffold devoid of cell and growth factor loading. A blank group and a non-elastic porous PCL scaffold group were used as controls. During the experiments, no significant surgical complications were observed in the experimental animals. Fig. 6a depicts the appearance of cartilage tissue after 12 weeks of implantation, as observed in photographs of cartilage tissue samples from the control group. The cartilage tissue samples from the control group were observed to be slightly filled, but with obvious unrepaired defects. The PCL group samples displayed a white interior (Fig. 6b). In contrast, defects repaired by PMCL20-DY samples were completely filled with tissue resembling cartilage (Fig. 6c).

Histological staining was also used to evaluate cartilage regeneration. In the staining of the blank group with Safranin-O (Fig. 6d), the filling of the defect was negative, indicating that no GAG had been deposited. The regenerated filling was fibrous-like rather than cartilage-like tissue. The H&E and Masson trichrome stains illustrated a similar trend (Fig. 6e and f). It was also demonstrated that the blank group was incapable of regenerating cartilage tissue through self-healing. The PCL group appeared negative when stained with Safranin-O (Fig. 6g–i), with fibrous tissue on the surface of the defect and a large number of void areas inside the defect. For defect repair, it was determined that normal cartilage tissue-related proteins were lacking. As with the PMCL20-DY group, the defect filling was positively stained by Safranin-O (Fig. 6j), indicating that the regenerated tissue was composed of hyaline cartilage matrix GAG with a blurred interface and good fusion with the native tissue (Fig. 6k and l). The pro-chondrogenic differentiation capacity of the PMCL20-DY scaffold may have, therefore, contributed to the fact that the regenerated cartilage was thicker than the normal cartilage layer.

As shown in Fig. 7, immunohistochemical staining of the tissue for types I, II, and X collagen was performed to investigate the regenerated tissue further. The defect filler in the control group was negative for COLII with mild COLI and COLX staining (Fig. 7a–c), indicating that COLII was not deposited on the regenerated tissue and there was no cartilage formation. The PCL group defect filling was marginally positive for COLII and predominantly positive for COLI and COLX (Fig. 7d–f), suggesting possible manifestations of osteoarthritis [71]. The PMCL20-DY group samples were predominantly stained with COLII, with no COLI or COLX staining observed (Fig. 7g–i), indicating adequate COLII production and outstanding cartilage regeneration. Implants for cartilage repair must be able to withstand the mechanically demanding joint environment [72]. Increasing evidence suggests that poor contact with the host tissue leads to resorption and poor integration [73]. It was demonstrated in this study that plastic PCL inhibited tissue penetration in a mechanically demanding joint environment, leading to the failure of cartilage repair. The expression of COLI and COLX suggested the presence of osteoarthritis, most likely because the PCL scaffold failed to act as a mechanical cushion. In contrast, the PMCL20-DY scaffold with fatigue-resistant elastic was able to adapt to the intensely stimulating mechanical environment of the defect with excellent biomechanical integration. It is, therefore, believed that a softer matrix and weaker adhesion on the matrix are more conducive to the formation of cell aggregates, thereby promoting optimal cartilage differentiation. The scaffold's specific pore size prevents vascular invasion and endochondral ossification, thereby preserving the cartilage phenotype. Accordingly, the PMCL20-DY scaffold successfully repaired the cartilage defect.

4. Conclusion

Herein, a new highly elastic porous scaffold with tunable mechanical properties was successfully prepared through double-terminated

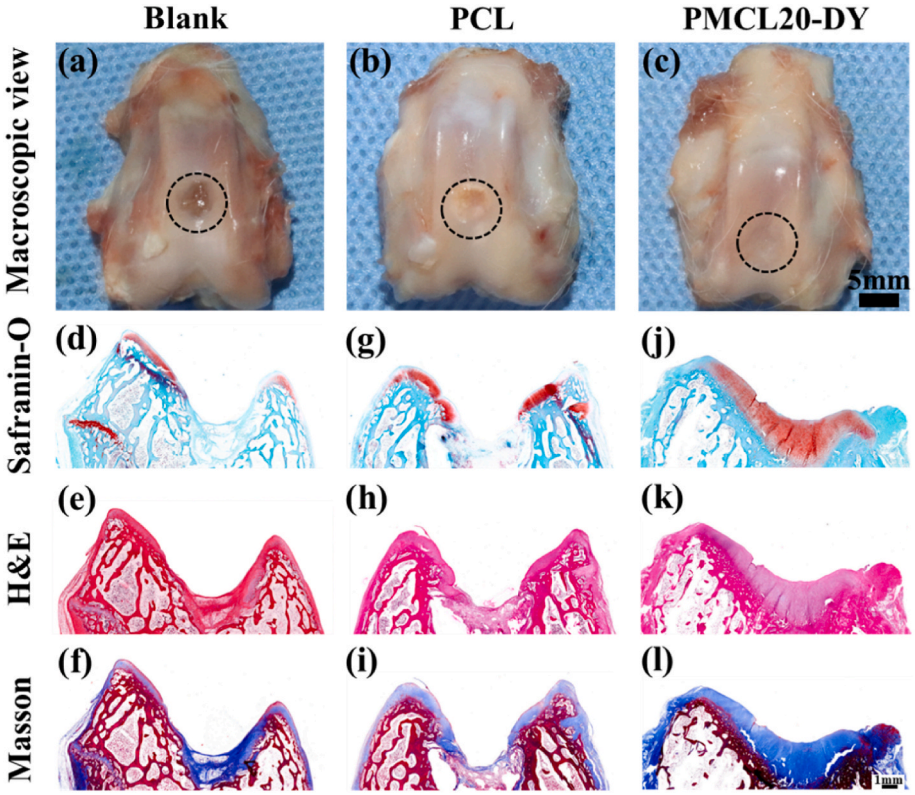

Fig. 6. Macroscopic view of the cartilage joints from Blank (a), PCL (b), and PMCL20-DY groups (c) at 12 weeks after surgery. Histological analyses: Safranin-O histological staining, H&E staining, and Masson's trichrome staining.

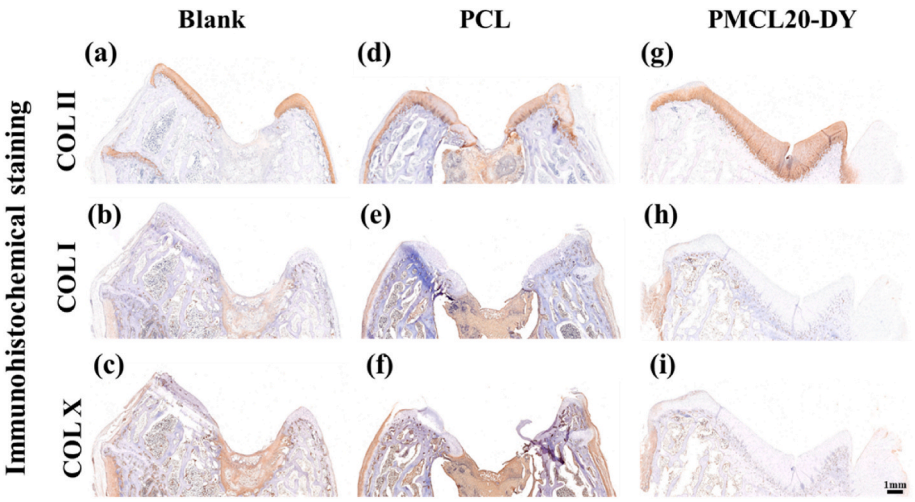

Fig. 7. Immumohistochemical staining of type II, type I and type X collagen of the regenerated tissue (Scale bar 1 mm).

alkynylation of amorphous liquid PMCL followed by thiol-yne photocrosslinking using a salt template method. Due to the polyester's liquid state at room temperature, toxic organic solvents could be avoided and the molding process was streamlined. Importantly, the modulus of the scaffold could be modified by three orders of magnitude, from 9.5 kPa to 115 kPa, by adjusting the cross-link density. The extremely low T_g (<-45 °C) and amorphous properties of the scaffold conferred excellent elasticity in its rubbery state at room temperature. Specifically, the PMCL20-DY porous scaffold was able to recover its original shape at 90% compressive strain with a rapid recovery rate of >500 mm min^{-1}. A very low energy loss coefficient of <0.1 resulted in superior fatigue resistance after 10,000 cycles at 70% compressive strain. Such high resilience of the scaffold allowed for minimally invasive loading and injection from a syringe. Moreover, the PMCL20-DY scaffolds with superior cytocompatibility and biodegradability stimulated chondrogenic differentiation of BMSCs in vitro. Furthermore, an in vivo articular cartilage defect model demonstrated its excellent cartilage regeneration capacity. Therefore, porous scaffolds with high elasticity and excellent fatigue resistance for withstanding dynamic loading may serve as potential implants for soft tissue regeneration.

Ethics approval

All the experimental procedures were approved and followed the rules and regulation strictly under Experimental Animal Ethics Committee of Shanghai Jiao Tong University School of Medicine Affiliated Ninth People's Hospital.

CRediT authorship contribution statement

Zhaochuang Wang: Data curation, Formal analysis, Investigation, Methodology, Roles/, Writing – original draft, Writing – review & editing. **Wenhao Zhang:** Formal analysis, Investigation, Resources. **Guo Bai:** Formal analysis, Investigation, Resources. **Qiaohui Lu:** Data curation, Formal analysis, Investigation, Methodology. **Xiaoyu Li:** Data curation, Investigation. **Yan Zhou:** Project administration, Resources, Validation. **Chi Yang:** Funding acquisition, Resources. **Yan Xiao:** Conceptualization, Funding acquisition, Project administration, Resources, Writing – review & editing. **Meidong Lang:** Conceptualization, Project administration, Supervision, Writing – review & editing.

Declaration of competing interest

The authors declare that they have no known competing financial interests or personal relationships that could have appeared to influence the work reported in this paper.

Acknowledgements

We are grateful to the financial support by the National Key Research and Development Program (2021YFB3800800), the National Natural Science Foundation of China (52273009), the National Natural Science Foundation of China (82271038) and the Interdisciplinary Program of Shanghai JiaoTong University (YG2022QN050).

Appendix A. Supplementary data

Supplementary data to this article can be found online at https://doi.org/10.1016/j.bioactmat.2023.05.020.

References

[1] R. Langer, J.P. Vacanti, Tissue engineering, Science 260 (5115) (1993) 920–926, https://doi.org/10.1126/science.8493529.
[2] A.K. Gaharwar, I. Singh, A. Khademhosseini, Engineered biomaterials for in situ tissue regeneration, Nat. Rev. Mater. 5 (9) (2020) 686–705, https://doi.org/10.1038/s41578-020-0209-x.
[3] N. Iqbal, A.S. Khan, A. Asif, M. Yar, J.W. Haycock, I.U. Rehman, Recent concepts in biodegradable polymers for tissue engineering paradigms: a critical review, Int. Mater. Rev. 64 (2) (2018) 91–126, https://doi.org/10.1080/09506608.2018.1460943.
[4] M.P. Nikolova, M.S. Chavali, Recent advances in biomaterials for 3D scaffolds: a review, Bioact. Mater. 4 (2019) 271–292, https://doi.org/10.1016/j.bioactmat.2019.10.005.
[5] Y. Wang, G.A. Ameer, B.J. Sheppard, R. Langer, A tough biodegradable elastomer, Nat. Biotechnol. 20 (2002) 602–606, https://doi.org/10.1038/nbt0602-602.
[6] A.M.J. Coenen, K.V. Bernaerts, J.A.W. Harings, S. Jockenhoevel, S. Ghazanfari, Elastic materials for tissue engineering applications: natural, synthetic, and hybrid polymers, Acta Biomater. 79 (2018) 60–82, https://doi.org/10.1016/j.actbio.2018.08.027.
[7] C. Xu, Y. Hong, Rational design of biodegradable thermoplastic polyurethanes for tissue repair, Bioact. Mater. 15 (2022) 250–271, https://doi.org/10.1016/j.bioactmat.2021.11.029.
[8] Y. Zhao, S. Song, X. Ren, J. Zhang, Q. Lin, Y. Zhao, Supramolecular adhesive hydrogels for tissue engineering applications, Chem. Rev. 122 (6) (2022) 5604–5640, https://doi.org/10.1021/acs.chemrev.1c00815.
[9] Q. Chen, S. Liang, G.A. Thouas, Elastomeric biomaterials for tissue engineering, Prog. Polym. Sci. 38 (3–4) (2013) 584–671, https://doi.org/10.1016/j.progpolymsci.2012.05.003.
[10] G.X. De Hoe, M.T. Zumstein, B.J. Tiegs, J.P. Brutman, K. McNeill, M. Sander, G. W. Coates, M.A. Hillmyer, Sustainable polyester elastomers from lactones: synthesis, properties, and enzymatic hydrolyzability, J. Am. Chem. Soc. 140 (3) (2018) 963–973, https://doi.org/10.1021/jacs.7b10173.
[11] S. Liffland, M.A. Hillmyer, Enhanced mechanical properties of aliphatic polyester thermoplastic elastomers through star block architectures, Macromolecules 54 (20) (2021) 9327–9340, https://doi.org/10.1021/acs.macromol.1c01357.
[12] B. Luo, Q. Zhou, W. Chen, L. Sun, L. Yang, Y. Guo, H. Liu, Z. Wu, R.E. Neisiany, X. Qin, J. Pan, Z. You, Nonadjacent wireless electrotherapy for tissue repair by a

3D-printed bioresorbable fully soft triboelectric nanogenerator, Nano Lett. (2023), https://doi.org/10.1021/acs.nanolett.3c00300.
[13] S. Chen, L. Sun, X. Zhou, Y. Guo, J. Song, S. Qian, Z. Liu, Q. Guan, E. Meade Jeffries, W. Liu, Y. Wang, C. He, Z. You, Mechanically and biologically skin-like elastomers for bio-integrated electronics, Nat. Commun. 11 (1) (2020) 1107, https://doi.org/10.1038/s41467-020-14446-2.
[14] H. Ye, K. Zhang, D. Kai, Z. Li, X.J. Loh, Polyester elastomers for soft tissue engineering, Chem. Soc. Rev. 47 (12) (2018) 4545–4580, https://doi.org/10.1039/c8cs00161h.
[15] S.H. Lee, B.S. Kim, S.H. Kim, S.W. Choi, S.I. Jeong, I.K. Kwon, S.W. Kang, J. Nikolovski, D.J. Mooney, Y.K. Han, Y.H. Kim, Elastic biodegradable poly (glycolide-co-caprolactone) scaffold for tissue engineering, J. Biomed. Mater. Res. A. 66 (1) (2003) 29–37, https://doi.org/10.1002/jbm.a.10497.
[16] W. Liu, Z. Feng, W. Ou-Yang, X. Pan, X. Wang, P. Huang, C. Zhang, D. Kong, W. Wang, 3D printing of implantable elastic PLCL copolymer scaffolds, Soft Matter 16 (8) (2020) 2141–2148, https://doi.org/10.1039/c9sm02396h.
[17] M. Zhu, Y. Wu, W. Li, X. Dong, H. Chang, K. Wang, P. Wu, J. Zhang, G. Fan, L. Wang, J. Liu, H. Wang, D. Kong, Biodegradable and elastomeric vascular grafts enable vascular remodeling, Biomaterials 183 (2018) 306–318, https://doi.org/10.1016/j.biomaterials.2018.08.063.
[18] E.S. Place, J.H. George, C.K. Williams, M.M. Stevens, Synthetic polymer scaffolds for tissue engineering, Chem. Soc. Rev. 38 (4) (2009) 1139–1151, https://doi.org/10.1039/b811392k.
[19] I.G. Kim, M.P. Hwang, P. Du, J. Ko, C.W. Ha, S.H. Do, K. Park, Bioactive cell-derived matrices combined with polymer mesh scaffold for osteogenesis and bone healing, Biomaterials 50 (2015) 75–86, https://doi.org/10.1016/j.biomaterials.2015.01.054.
[20] M. Xie, L. Wang, B. Guo, Z. Wang, Y.E. Chen, P.X. Ma, Ductile electroactive biodegradable hyperbranched polylactide copolymers enhancing myoblast differentiation, Biomaterials 71 (2015) 158–167, https://doi.org/10.1016/j.biomaterials.2015.08.042.
[21] S. Xu, J. Liu, L. Zhang, F. Yang, P. Tang, D. Wu, Effects of HAp and TCP in constructing tissue engineering scaffolds for bone repair, J. Mater. Chem. B 5 (30) (2017) 6110–6118, https://doi.org/10.1039/c7tb00790f.
[22] T. Hu, Y. Wu, X. Zhao, L. Wang, L. Bi, P.X. Ma, B. Guo, Micropatterned, electroactive, and biodegradable poly(glycerol sebacate)-aniline trimer elastomer for cardiac tissue engineering, Chem. Eng. J. 366 (2019) 208–222, https://doi.org/10.1016/j.cej.2019.02.072.
[23] Y. Xu, Y. Guo, Y. Li, Y. Huo, Y. She, H. Li, Z. Jia, G. Jiang, G. Zhou, Z. You, L. Duan, Biomimetic trachea regeneration using a modular ring strategy based on poly (sebacoyl diglyceride)/polycaprolactone for segmental trachea defect repair, Adv. Funct. Mater. 30 (42) (2020), 2004276, https://doi.org/10.1002/adfm.202004276.
[24] J. Fu, M. Wang, I. De Vlaminck, Y. Wang, Thick PCL fibers improving host remodeling of PGS-PCL composite grafts implanted in rat common carotid arteries, Small 16 (52) (2020), e2004133, https://doi.org/10.1002/smll.202004133.
[25] H. Xuan, H. Hu, C. Geng, J. Song, Y. Shen, D. Lei, Q. Guan, S. Zhao, Z. You, Biofunctionalized chondrogenic shape-memory ternary scaffolds for efficient cell-free cartilage regeneration, Acta Biomater. 105 (2020) 97–110, https://doi.org/10.1016/j.actbio.2020.01.015.
[26] J. Yang, A.R. Webb, S.J. Pickerill, G. Hageman, G.A. Ameer, Synthesis and evaluation of poly(diol citrate) biodegradable elastomers, Biomaterials 27 (9) (2006) 1889–1898, https://doi.org/10.1016/j.biomaterials.2005.05.106.
[27] W. Chen, W. Xiao, X. Liu, P. Yuan, S. Zhang, Y. Wang, W. Wu, Pharmacological manipulation of macrophage autophagy effectively rejuvenates the regenerative potential of biodegrading vascular graft in aging body, Bioact. Mater. 11 (2022) 283–299, https://doi.org/10.1016/j.bioactmat.2021.09.027.
[28] S. Huang, D. Lei, Q. Yang, Y. Yang, C. Jiang, H. Shi, B. Qian, Q. Long, W. Chen, Y. Chen, L. Zhu, W. Yang, L. Wang, W. Hai, Q. Zhao, Z. You, X. Ye, A perfusable, multifunctional epicardial device improves cardiac function and tissue repair, Nat. Med. 27 (3) (2021) 480–490, https://doi.org/10.1038/s41591-021-01279-9.
[29] L. Zhang, J. Liang, C. Jiang, Z. Liu, L. Sun, S. Chen, H. Xuan, D. Lei, Q. Guan, X. Ye, Z. You, Peptidoglycan-inspired autonomous ultrafast self-healing bio-friendly elastomers for bio-integrated electronics, Natl. Sci. Rev. 8 (5) (2021), https://doi.org/10.1093/nsr/nwaa154 nwaa154.
[30] J. Fu, X. Ding, C.E.T. Stowell, Y.L. Wu, Y. Wang, Slow degrading poly(glycerol sebacate) derivatives improve vascular graft remodeling in a rat carotid artery interposition model, Biomaterials 257 (2020), 120251, https://doi.org/10.1016/j.biomaterials.2020.120251.
[31] Y. Yang, D. Lei, S. Huang, Q. Yang, B. Song, Y. Guo, A. Shen, Z. Yuan, S. Li, F. L. Qing, X. Ye, Z. You, Q. Zhao, Elastic 3D-printed hybrid polymeric scaffold improves cardiac remodeling after myocardial infarction, Adv. Healthc. Mater. 8 (10) (2019), e1900065, https://doi.org/10.1002/adhm.201900065.
[32] Y.C. Yeh, C.B. Highley, L. Ouyang, J.A. Burdick, 3D printing of photocurable poly (glycerol sebacate) elastomers, Biofabrication 8 (4) (2016), 045004, https://doi.org/10.1088/1758-5090/8/4/045004.
[33] P. Wang, D.B. Berry, Z. Song, W. Kiratitanaporn, J. Schimelman, A. Moran, F. He, B. Xi, S. Cai, S. Chen, 3D printing of a biocompatible double network elastomer with digital control of mechanical properties, Adv. Funct. Mater. 30 (14) (2020), 1910391, https://doi.org/10.1002/adfm.201910391.
[34] J. Wang, J. Li, X. Wang, Q. Cheng, Y. Weng, J. Ren, Synthesis and properties of UV-curable polyester acrylate resins from biodegradable poly(l-lactide) and poly (ε-caprolactone), React. Funct. Polym. 155 (2020), 104695, https://doi.org/10.1016/j.reactfunctpolym.2020.104695.
[35] T. Yao, H. Chen, R. Wang, R. Rivero, F. Wang, L. Kessels, S.M. Agten, T. M. Hackeng, T. Wolfs, D. Fan, M.B. Baker, L. Moroni, Thiol-ene conjugation of VEGF peptide to electrospun scaffolds as potential application for angiogenesis, Bioact. Mater. 20 (2023) 306–317, https://doi.org/10.1016/j.bioactmat.2022.05.029.
[36] A. Oesterreicher, J. Wiener, M. Roth, A. Moser, R. Gmeiner, M. Edler, G. Pinter, T. Griesser, Tough and degradable photopolymers derived from alkyne monomers for 3D printing of biomedical materials, Polym. Chem. 7 (32) (2016) 5169–5180, https://doi.org/10.1039/c6py01132b.
[37] S. Seiffert, Origin of nanostructural inhomogeneity in polymer-network gels, Polym. Chem. 8 (31) (2017) 4472–4487, https://doi.org/10.1039/c7py01035d.
[38] B.D. Fairbanks, M.P. Schwartz, A.E. Halevi, C.R. Nuttelman, C.N. Bowman, K. S. Anseth, A versatile synthetic extracellular matrix mimic via thiol-norbornene photopolymerization, Adv. Mater. 21 (48) (2009) 5005–5010, https://doi.org/10.1002/adma.200901808.
[39] C.C. Lin, A. Raza, H. Shih, PEG hydrogels formed by thiol-ene photo-click chemistry and their effect on the formation and recovery of insulin-secreting cell spheroids, Biomaterials 32 (36) (2011) 9685–9695, https://doi.org/10.1016/j.biomaterials.2011.08.083.
[40] A. Massi, D. Nanni, Thiol-yne coupling: revisiting old concepts as a breakthrough for up-to-date applications, Org. Biomol. Chem. 10 (19) (2012) 3791–3807, https://doi.org/10.1039/c2ob25217a.
[41] J. Guo, Z. Xie, R.T. Tran, D. Xie, D. Jin, X. Bai, J. Yang, Click chemistry plays a dual role in biodegradable polymer design, Adv. Mater. 26 (12) (2014) 1906–1911, https://doi.org/10.1002/adma.201305162.
[42] Y.C. Yeh, L. Ouyang, C.B. Highley, J.A. Burdick, Norbornene-modified poly (glycerol sebacate) as a photocurable and biodegradable elastomer, Polym. Chem. 8 (34) (2017) 5091–5099, https://doi.org/10.1039/c7py00323d.
[43] Q. Thijssen, L. Parmentier, E. Augustyniak, P. Mouthuy, S. Van Vlierberghe, From chain growth to step growth polymerization of photoreactive poly-ε-caprolactone: the network topology of bioresorbable networks as tool in tissue engineering, Adv. Funct. Mater. 32 (20) (2022), 2108869, https://doi.org/10.1002/adfm.202108869.
[44] Y. Xiao, S. Lang, M. Zhou, J. Qin, R. Yin, J. Gao, A. Heise, M. Lang, A highly stretchable bioelastomer prepared by UV curing of liquid-like poly(4-methyl-epsilon-caprolactone) precursors, J. Mater. Chem. B 5 (3) (2017) 595–603, https://doi.org/10.1039/c6tb02507b.
[45] Y. Xiao, M. Zhou, M. Zhang, W. Liu, Y. Zhou, M. Lang, Hepatocyte culture on 3D porous scaffolds of PCL/PMCL, Colloids Surf., B 173 (2019) 185–193, https://doi.org/10.1016/j.colsurfb.2018.09.064.
[46] L. Wang, Y. Qiu, H. Lv, Y. Si, L. Liu, Q. Zhang, J. Cao, J. Yu, X. Li, B. Ding, 3D superelastic scaffolds constructed from flexible inorganic nanofibers with self-fitting capability and tailorable gradient for bone regeneration, Adv. Funct. Mater. 29 (31) (2019), 1901407, https://doi.org/10.1002/adfm.201901407.
[47] M.A. Daniele, A.A. Adams, J. Naciri, S.H. North, F.S. Ligler, Interpenetrating networks based on gelatin methacrylamide and PEG formed using concurrent thiol click chemistries for hydrogel tissue engineering scaffolds, Biomaterials 35 (6) (2014) 1845–1856, https://doi.org/10.1016/j.biomaterials.2013.11.009.
[48] X. Huang, S. Nakagawa, X. Li, M. Shibayama, N. Yoshie, A simple and versatile method for the construction of nearly ideal polymer networks, Angew. Chem. Int. Ed. 59 (24) (2020) 9646–9652, https://doi.org/10.1002/anie.202001271.
[49] C.E. Hoyle, C.N. Bowman, Thiol-ene click chemistry, Angew. Chem. Int. Ed. 49 (9) (2010) 1540–1573, https://doi.org/10.1002/anie.200903924.
[50] C. Yu, J. Schimelman, P. Wang, K.L. Miller, X. Ma, S. You, J. Guan, B. Sun, W. Zhu, S. Chen, Photopolymerizable biomaterials and light-based 3D printing strategies for biomedical applications, Chem. Rev. 120 (19) (2020) 10695–10743, https://doi.org/10.1021/acs.chemrev.9b00810.
[51] J.J. Roberts, S.J. Bryant, Comparison of photopolymerizable thiol-ene PEG and acrylate-based PEG hydrogels for cartilage development, Biomaterials 34 (38) (2013) 9969–9979, https://doi.org/10.1016/j.biomaterials.2013.09.020.
[52] X. Jing, H.Y. Mi, T. Cordie, M. Salick, X. Peng, L. Turng, Fabrication of porous poly (ε-caprolactone) scaffolds containing chitosan nanofibers by combining extrusion foaming, leaching, and freeze-drying methods, Ind. Eng. Chem. Res. 53 (46) (2014) 17909–17918, https://doi.org/10.1021/ie5034073.
[53] H.Y. Mi, X. Jing, M.x.R. Salick, L. Turng, X. Peng, Fabrication of thermoplastic polyurethane tissue engineering scaffold by combining microcellular injection molding and particle leaching, J. Mater. Res. 29 (8) (2014) 911–922, https://doi.org/10.1557/jmr.2014.67.
[54] R. Yuan, Y. Zhou, X. Lu, Z. Dong, Q. Lu, Rigid and flexible polyimide aerogels with less fatigue for use in harsh conditions, Chem. Eng. J. 428 (2022), 131193, https://doi.org/10.1016/j.cej.2021.131193.
[55] L. Dou, X. Cheng, X. Zhang, Y. Si, J. Yu, B. Ding, Temperature-invariant superelastic, fatigue resistant, and binary-network structured silica nanofibrous aerogels for thermal superinsulation, J. Mater. Chem. A. 8 (16) (2020) 7775–7783, https://doi.org/10.1039/d0ta01092h.
[56] H. Liu, X. Chen, Y. Zheng, D. Zhang, Y. Zhao, C. Wang, C. Pan, C. Liu, C. Shen, Lightweight, superelastic, and hydrophobic polyimide nanofiber/MXene composite aerogel for wearable piezoresistive sensor and oil/water separation applications, Adv. Funct. Mater. 31 (13) (2021), 2008006, https://doi.org/10.1002/adfm.202008006.
[57] G. Du, G. Gao, R. Hou, Y. Cheng, T. Chen, J. Fu, B. Fei, Tough and fatigue resistant biomimetic hydrogels of interlaced self-assembled conjugated polymer belts with a polyelectrolyte network, Chem. Mater. 26 (11) (2014) 3522–3529, https://doi.org/10.1021/cm501095s.
[58] Q. Zhang, Z. Xu, X. Zhang, C. Liu, R. Yang, Y. Sun, Y. Zhang, W. Liu, 3D printed high-strength supramolecular polymer hydrogel-cushioned radially and circumferentially oriented meniscus substitute, Adv. Funct. Mater. 32 (23) (2022), 2200360, https://doi.org/10.1002/adfm.202200360.

[59] J. Ai, K. Li, J. Li, F. Yu, J. Ma, Super flexible, fatigue resistant, self-healing PVA/xylan/borax hydrogel with dual-crosslinked network, Int. J. Biol. Macromol. 172 (2021) 66–73, https://doi.org/10.1016/j.ijbiomac.2021.01.038.
[60] C. Chen, J. Song, J. Cheng, Z. Pang, W. Gan, G. Chen, Y. Kuang, H. Huang, U. Ray, T. Li, L. Hu, Highly elastic hydrated cellulosic materials with durable compressibility and tunable conductivity, ACS Nano 14 (12) (2020) 16723–16734, https://doi.org/10.1021/acsnano.0c04298.
[61] L. Wang, Y. Qiu, Y. Guo, Y. Si, L. Liu, J. Cao, J. Yu, X. Li, Q. Zhang, B. Ding, Smart, elastic, and nanofiber-based 3D scaffolds with self-deploying capability for osteoporotic bone regeneration, Nano Lett. 19 (12) (2019) 9112–9120, https://doi.org/10.1021/acs.nanolett.9b04313.
[62] H.L. Gao, Y.B. Zhu, L.B. Mao, F.C. Wang, X.S. Luo, Y.Y. Liu, Y. Lu, Z. Pan, J. Ge, W. Shen, Y.R. Zheng, L. Xu, L.J. Wang, W.H. Xu, H.A. Wu, S.H. Yu, Super-elastic and fatigue resistant carbon material with lamellar multi-arch microstructure, Nat. Commun. 7 (2016), 12920, https://doi.org/10.1038/ncomms12920.
[63] N. Ashammakhi, S. Ahadian, M.A. Darabi, M. El Tahchi, J. Lee, K. Suthiwanich, A. Sheikhi, M.R. Dokmeci, R. Oklu, A. Khademhosseini, Minimally invasive and regenerative therapeutics, Adv. Mater. 31 (1) (2019), e1804041, https://doi.org/10.1002/adma.201804041.
[64] H. Madry, L. Gao, A. Rey-Rico, J.K. Venkatesan, K. Muller-Brandt, X. Cai, L. Goebel, G. Schmitt, S. Speicher-Mentges, D. Zurakowski, M.D. Menger, M.W. Laschke, M. Cucchiarini, Thermosensitive hydrogel based on PEO-PPO-PEO poloxamers for a controlled in situ release of recombinant adeno-associated viral vectors for effective gene therapy of cartilage defects, Adv. Mater. 32 (2) (2020), e1906508, https://doi.org/10.1002/adma.201906508.
[65] J. Delaey, P. Dubruel, S. Van Vlierberghe, Shape-memory polymers for biomedical applications, Adv. Funct. Mater. 30 (44) (2020), 1909047, https://doi.org/10.1002/adfm.201909047.
[66] M. Montgomery, S. Ahadian, L. Davenport Huyer, M. Lo Rito, R.A. Civitarese, R. D. Vanderlaan, J. Wu, L.A. Reis, A. Momen, S. Akbari, A. Pahnke, R.K. Li, C. A. Caldarone, M. Radisic, Flexible shape-memory scaffold for minimally invasive delivery of functional tissues, Nat. Mater. 16 (10) (2017) 1038–1046, https://doi.org/10.1038/nmat4956.
[67] C.X.F. Lam, S.H. Teoh, D.W. Hutmacher, Comparison of the degradation of polycaprolactone and polycaprolactone–(β-tricalcium phosphate) scaffolds in alkaline medium, Polym. Int. 56 (6) (2007) 718–728, https://doi.org/10.1002/pi.2195.
[68] Y. Wang, U.J. Kim, D.J. Blasioli, H.J. Kim, D.L. Kaplan, In vitro cartilage tissue engineering with 3D porous aqueous-derived silk scaffolds and mesenchymal stem cells, Biomaterials 26 (34) (2005) 7082–7094, https://doi.org/10.1016/j.biomaterials.2005.05.022.
[69] M.J. Gupte, W.B. Swanson, J. Hu, X. Jin, H. Ma, Z. Zhang, Z. Liu, K. Feng, G. Feng, G. Xiao, N. Hatch, Y. Mishina, P.X. Ma, Pore size directs bone marrow stromal cell fate and tissue regeneration in nanofibrous macroporous scaffolds by mediating vascularization, Acta Biomater. 82 (2018) 1–11, https://doi.org/10.1016/j.actbio.2018.10.016.
[70] M. Chen, Y. Zhang, Y. Zhou, Y. Zhang, M. Lang, Z. Ye, W.S. Tan, Pendant small functional groups on poly(ε-caprolactone) substrate modulate adhesion, proliferation and differentiation of human mesenchymal stem cells, Colloids Surf., B 134 (2015) 322–331, https://doi.org/10.1016/j.colsurfb.2015.07.018.
[71] D. Lin, B. Cai, L. Wang, L. Cai, Z. Wang, J. Xie, Q.X. Lv, Y. Yuan, C. Liu, S.G. Shen, A viscoelastic PEGylated poly(glycerol sebacate)-based bilayer scaffold for cartilage regeneration in full-thickness osteochondral defect, Biomaterials 253 (2020), 120095, https://doi.org/10.1016/j.biomaterials.2020.120095.
[72] J.K. Lee, L.W. Huwe, N. Paschos, A. Aryaei, C.A. Gegg, J.C. Hu, K.A. Athanasiou, Tension stimulation drives tissue formation in scaffold-free systems, Nat. Mater. 16 (8) (2017) 864–873, https://doi.org/10.1038/nmat4917.
[73] S. Yodmuang, H. Guo, C. Brial, R.F. Warren, P.A. Torzilli, T. Chen, S.A. Maher, Effect of interface mechanical discontinuities on scaffold-cartilage integration, J. Orthop. Res. 37 (4) (2019) 845–854, https://doi.org/10.1002/jor.24238.